Diurnal carbon monoxide observed from a geostationary infrared hyperspectral sounder: First result from GIIRS onboard FY-4B

Zhao-Cheng Zeng[1], Lu Lee[2], Chengli Qi[2]

[1]School of Earth and Space Sciences, Peking University, Beijing 100871, China

5 [2]Innovation Center for FengYun Meteorological Satellite, Key Laboratory of Radiometric Calibration and Validation for Environmental Satellites, National Satellite Meteorological Center, China Meteorological Administration, Beijing 100081, China

Correspondence to: Z.-C. Zeng (zczeng@pku.edu.cn)

Abstract. The Geostationary Interferometric Infrared Sounder (GIIRS) onboard FengYun-4 series satellites is the world's first

10 geostationary hyperspectral infrared sounder. With hyperspectral measurement covering the carbon monoxide (CO) absorption window around 2150 cm^{-1}, GIIRS provides a unique opportunity for monitoring the diurnal variabilities of atmospheric CO over East Asia. In this study, we develop the FengYun Geostationary satellite Atmospheric Infrared Retrieval (FY-GeoAIR) algorithm to retrieve the CO profiles from FY-4B/GIIRS data and provide CO maps at a spatial resolution of 12 km and a temporal resolution of 2 hours. The performance of the algorithm is first evaluated by conducting retrieval experiments using

15 simulated synthetic spectra. The result shows that the GIIRS data provide significant information for constraining CO profiles. The degree of freedom for signal (DOFS) and retrieval error are both significantly correlated with thermal contrast (TC), the temperature difference between the surface and the lower atmosphere. Retrieval results from one month of GIIRS spectra in July 2022 show that the DOFS for the majority is between 0.6 and 1.2 for the CO total column and between 0 and 0.25 for the bottom 0-1 km layer. Consistent with CO retrievals from low-earth-orbit (LEO) infrared sounders, the largest observation

20 sensitivity, as quantified by the averaging kernel (AK), is in the free troposphere at around 3-6 km. The diurnal changes in DOFS and vertical sensitivity of observation are primarily driven by the diurnal TC variabilities. Finally, we compare the CO total columns between GIIRS and IASI and find that the two datasets show good consistency in capturing the daily variabilities. This study demonstrates the capability of GIIRS in observing the diurnal CO changes in East Asia, which will have great potential in improving local and global air quality and climate research.

1 Introduction

Observing atmospheric composition from space provides critical data for forecasting air quality, assessing climate change, and monitoring the long-term variabilities in tropospheric and stratospheric compositions. In the last two decades, satellite-borne instruments onboard polar-orbiting satellites in Low-Earth Orbit (LEO) have demonstrated their full capabilities in observing the atmospheric composition (**e.g., Clerbaux et al., 2003; Crevoisier et al., 2014; Shephard et al., 2015; Buchwitz et al.,**

30 **2005; Borsdorff et al., 2018**). However, a single LEO satellite has a revisit time of 12 hours over the equator. Only one (for

near-infrared or UV–visible instrument) or two (for thermal infrared sounder) observations are available each day for the same spot. Critical information on the diurnal cycle of atmospheric composition is, however, not available from LEO satellites. As an important advancement over current LEO instruments, measurements from geostationary (GEO) orbit can provide contiguous coverage with high spatial resolution and a revisit time of 1-2 hours, which would provide breakthrough

35 measurements for numerical weather prediction and support high-temporal-resolution air quality forecasting (**Schmit et al., 2009**).

The Geostationary Interferometric Infrared Sounder (GIIRS) onboard FengYun-4 series satellites, launched in 2016 (FY-4A) and 2021 (FY-4B), respectively, is the world's first geostationary hyperspectral infrared sounder (**Yang et al., 2017**). With a spectral resolution of 0.625 cm^{-1}, similar to current LEO satellites, GIIRS provides a unique opportunity for observing the

40 diurnal variabilities of atmospheric composition over East Asia, as has been demonstrated in retrieving atmospheric ammonia (**Clarisse et al., 2021**). Existing on-orbit GEO instruments for observing air quality also include the Geostationary Environment Monitoring Spectrometer (GEMS) by South Korea which was launched in Feb. 2020. GEMS was designed to measure air quality in Asia using ultraviolet and visible (UV/VIS) bands (**Kim et al., 2020**). Future GEO missions with hyperspectral capabilities include ESA's Sentinel-4 mission onboard the Meteosat Third Generation Sounder platform, which

45 is made up of the thermal Infrared Sounder (IRS) for providing profiles of temperature and humidity and the Ultraviolet Visible Near-infrared (UVN) spectrometer for monitoring air quality trace gases and aerosols in Europe (**Ingmann et al., 2012; Holmlund et al., 2021**), and NASA's Tropospheric Emissions: Monitoring of Pollution (TEMPO; **Zoogman et al., 2017**) that will track air quality in North America. In addition, the to-be-launched greenhouse gas targeted mission: Geostationary Carbon Cycle Observatory (GeoCarb) by NASA was designed to measure carbon dioxide (CO_2), methane (CH_4), and carbon monoxide

50 (CO) throughout the Americas (**Polonsky et al., 2014**).

As an important trace gas for understanding air quality and climate forcing, CO is a direct product of incomplete combustion primarily from biomass and fossil fuel on the surface and a by-product of oxidation of CH_4 and non-methane hydrocarbons in the atmosphere (**Brenninkmeijer and Novelli, 2003**). Being a precursor to the formation of tropospheric ozone, CO also plays an important role in tropospheric chemistry (**Chin et al., 1994**). Because of its low background concentration and moderately

55 long lifetime (weeks to months) in the troposphere, CO is an effective tracer for the long-range transport of pollution (**Forster et al., 2001**) and carbon emissions (**Gamnitzer et al., 2006**). Nadir observation of CO from space has been providing long-term global coverage from both thermal (TIR) and near-infrared (NIR) instruments. One of the earliest attempts to retrieve atmospheric CO was made by the Interferometric Monitor of Greenhouse gases (IMG) onboard the Japanese ADEOS satellite (**Kobayashi et al., 1999**). From the early 2000s, the Measurements Of Pollution in The Troposphere (MOPITT) instrument

60 onboard NASA's Terra satellite launched was the first to provide routine global maps of CO daily (**Deeter et al., 2003**). Following missions with CO nadir observation capability includes the Infrared Atmospheric Sounding Interferometer (IASI) onboard Metop-A/B (**Hurtmans et al., 2012**), the Scanning Imaging Absorption Spectrometer for Atmospheric Chartography (SCIAMACHY) onboard the European ENVISAT satellite (**Buchwitz et al., 2005**), the Tropospheric Emission Sounder (TES) onboard NASA's Aura satellite (**Luo et al., 2007**), and the Cross-track Infrared Sounder (CrIS) onboard the Suomi National

65 Polar-orbiting Partnership platform (**Goldberg et al., 2013; Gambacorta et al., 2014**). More recently, TROPOMI and GOSAT-2, covering the NIR spectra, provides additional daily global views of CO (**Borsdorff et al., 2018; Noël et al., 2022**). However, none of the current instruments and missions provide diurnal CO measurements with high temporal resolution from a GEO platform.

In this study, we report the first result of diurnal CO retrieved from the hyperspectral infrared measurements by the GIIRS
70 using the Feng-Yun Geostationary satellite Atmospheric Infrared Retrieval (FY-GeoAIR) algorithm. The retrieval algorithm uses the absorption feature of CO's fundamental 1-0 rotation-vibration band centered around 4.7 μm (2150 cm^{-1}), which allows the measurement to be made during the daytime and the nighttime and provides important vertical information from the retrieval (**Crevoisier, 2018**). The clear-sky CO retrievals and uncertainties are produced as well as the averaging kernel (AK) matrix for each retrieval that quantifies its vertical observation sensitivity and information content.

75 This paper is organized as follows. In **Sect. 2**, the GIIRS instrument and the observed spectra data are introduced. In **Sect. 3**, we describe the details of the forward model based on radiative transfer and the inverse model based on optimal estimation theory. We show results from a simulation experiment in **Sect. 4** to assess the performance of the retrieval algorithm. Results of CO retrievals from applying the algorithm to GIIRS spectra in July of 2022 are demonstrated in **Sect. 5**, followed by discussions and conclusions in **Sect. 6** and **Sect. 7**, respectively.

2 The Geostationary Interferometric Infrared Sounder (GIIRS)

2.1 GIIRS

The FY-4 satellites series are China's second-generation geostationary meteorological satellites with improved capabilities for weather and environmental monitoring. FY-4B, the second satellite in the FY-4 series was launched in June 2021, following FY-4A which was launched in December 2016. The GIIRS onboard FY-4 is an infrared Fourier transform spectrometer based
85 on a Michelson interferometer, also the first space-borne interferometer in geostationary orbit, primarily aiming to measure the three-dimensional atmospheric structure of temperature and water vapor for the numerical weather forecast. FY-4B/GIIRS is located at an altitude of 35,786 km above the equator at 123.5°E after launch and was relocated to 133°E after April 11, 2022. The observation domain of FY-4B/GIIRS is mostly over East Asia, with a focus on China, as shown in **Fig. 1(a).** Climatological maps of surface pressure and temperature of the observation domain are shown in **Fig. A1** in the **Appendix**.
90 FY-4B/GIIRS makes routine observations of the full region every 2 hours and 12 times per day (starting at 0, 2, 4, …, 22h UTC, respectively). Note that the starting hours have been changed to 1, 3, 5, …, 23h UTC after September 06, 2022. Each full region observation comprises 12 horizontal scans, and each scan sequence consists of 27 fields-of-regards (FORs) plus one deep space (DS) and one internal calibration target (ICT) measurement. The DS and ICT measurements are used as two known radiation sources to radiometrically calibrate the Earth-observing spectra. One full region coverage takes about 1.5
95 hours, and in the following 0.5 hours of each 2-hour observing cycle, the sounder is operated in the external calibration mode

for instrument performance validation. The layout of the 2-dimension infrared plane array detector for each FOR is shown in **Fig. 1(b)**. The detector has 16×8 pixels with a sparse arrangement. A pixel spans 120 μm and the field of view (FOV) is 336 μrad. The spatial sampling on the Earth's surface is about 12 km at Nadir. The observed Earth's upwelling infrared radiation covers two spectra regions: long-wave IR band from 680 to 1130 cm^{-1} and mid-wave IR band from 1650 to 2250 cm^{-1} with a

100   spectral resolution of 0.625 cm^{-1}. With low instrument noise and a high spectral resolution and range similar to current LEO IR sounders, GIIRS is in principle capable of measuring trace gases, including CO, and providing full day-night diurnal cycle observations. **Fig. 1(c)** shows an example of GIIRS spectra for the CO retrieval window from 2143 to 2181.25 cm^{-1}, and the Jacobian for CO and the interference gas H_2O to demonstrate their contribution to the absorption features in the original spectra.

2.2 Assessment of GIIRS pre-launch instrument noise

105   For predicting FY-4B/GIIRS's post-launch performance, a series of blackbody calibration experiments have been conducted before launch in a laboratory thermal vacuum tank to evaluate the radiometric performances of the GIIRS instrument. As described in detail by **Li et al. (2022)**, the evaluation results showed that the noise equivalent differential radiance (NedR) on average in the mid-wave IR bands, covering the CO absorption channel, is less than 0.1mW/($m^2 \cdot sr \cdot cm^{-1}$). As for the radiometric calibration, the mid-wave IR band is susceptible to noise when the instrument is used to observe low-temperature targets.

110   Nevertheless, the radiometric noise in brightness temperature also met the 0.7K requirement in the range of 260-315K, which is comparable to existing infrared sounders. As a result, low instrument noise for GIIRS makes it possible to provide strong constrain on retrieving CO vertical distribution.

2.3 Filtering of cloudy GIIRS pixels

Only clear-sky or near-clear-sky pixels are considered in the retrieval algorithm. To filter out cloudy pixels, we adopted the

115   higher-resolution (4 km) level-2 cloud mask (CLM) data product from the Advanced Geostationary Radiation Imager (AGRI) onboard FY-4B. AGRI uses multispectral threshold algorithms based on different spectral characteristics of VIS, NIR, and TIR bands under cloudy and clear conditions to obtain cloud mask information (**Lai et al., 2019**). The cloud mask of AGRI classifies pixels into four categories: clear, probably clear, probably cloudy, and cloudy. We collocated the GIIRS and AGRI footprints and assigned the GIIRS to be clear or near-clear when at least 80% of the collocated AGRI pixels are labeled as

120   clear or probably clear.

125

(a)

(b)

(c)
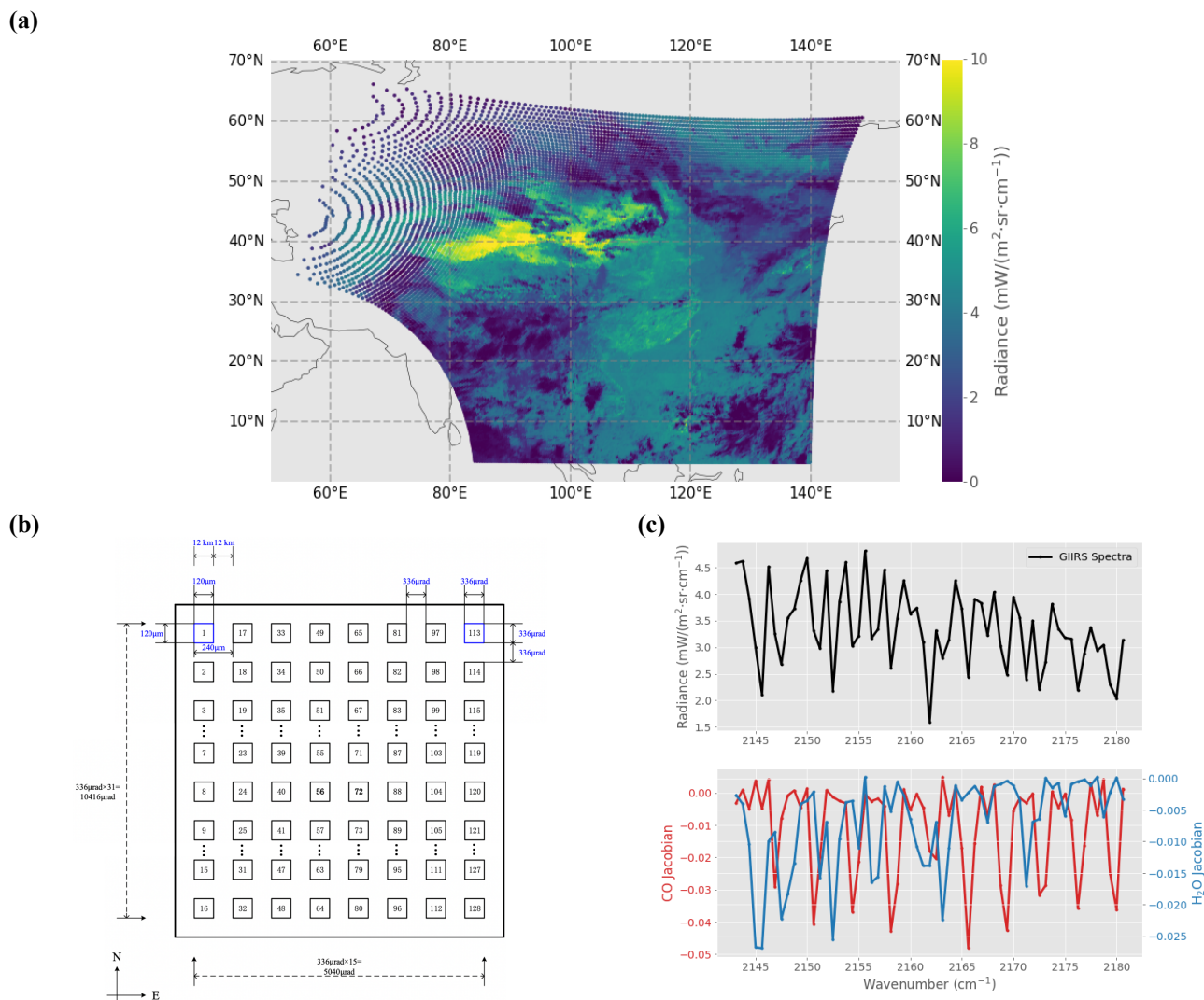
Figure 1: (a) FY-4B/GIIRS observation coverage from the tropics to ~60°N, and from ~60°E to ~140°E. The footprints on the left are sparse because of the geometric effect related to the large viewing zenith angle. The color denotes the observed radiance at 2132.5 cm^{-1} in hour 04-05 UTC on July 24, 2022, as an example; (b) The layout of the 2-dimension infrared plane array detector of GIIRS. The detector has 16×8 pixels with a sparse arrangement. A pixel spans 120 μm and the field of view is 336 μrad. The spatial sampling on the Earth's surface is about 12 km at Nadir; (c) (top) An example of GIIRS spectra in the CO retrieval window from 2143 to 2181.25 cm^{-1}; (bottom) Jacobian for CO and the interference gas H$_2$O in the 4th layer, where the averaging kernel value peaks.

3 The forward model in FY-GeoAIR for simulating observed spectra

130 An accurate radiative transfer (RT) model for simulating spectra is a prerequisite for constructing the inversion system for atmospheric composition retrieval. The thermal RT model is built based on radiative transfer theory with inputs of (1) atmospheric state including profiles of temperature, water vapor, atmospheric composition, and surface features; (2) the instrumental specifications, such as instrument spectral response function, and observing geometries; (3) spectroscopic database for computing the absorption cross-sections of gas molecules.

135 ### 3.1 Radiative transfer in the thermal infrared

The upwelling spectral radiance observed by GIIRS can be computed by integrating the RT Equation (1), which includes the same processes as the forward RT models by TES (**Clough et al., 2006**) and IASI (**Hurtmans et al., 2012**). Under clear conditions, scattering by clouds and aerosols can be ignored. For the CO absorption window around 2150 cm⁻¹, the surface reflected solar radiation accounts for several percent in the total upwelling radiance and, therefore, cannot be neglected. The

140 upwelling radiance received by a nadir-viewing satellite includes four main components: (a) surface emission (1st term in the r.h.s. of **Eq. (2)**); (b) upwelling atmospheric emission from the bottom- to the top- of the atmosphere [2nd term in the r.h.s. of **Eq. (1)**]; (c) surface-reflected downwelling atmospheric emission [2nd term in the r.h.s. of **Eq. (2)**]; and (d) surface-reflected solar radiation [3rd term in the r.h.s. of **Eq. (2)**]. All of these radiation sources are attenuated by the atmosphere. The RT Equation is given by:

145 $$I_\nu^\uparrow(\tau = 0, \mu) = I_\nu^\uparrow(\tau_\nu^*, \mu) \cdot T_\nu\left(\frac{\tau_\nu^*}{\mu}\right) + \int_0^{\tau_\nu^*} B_\nu(t(\tau')) \cdot \frac{\partial T_\nu\left(\frac{\tau'}{\mu}\right)}{\partial \tau'} d\tau' ,$$ (1)

and $I_\nu^\uparrow(\tau_\nu^*, \mu)$ is the upwelling radiance from the surface layer comprising three sub-processes given by:

$$I_\nu^\uparrow(\tau_\nu^*, \mu) = \epsilon_\nu \cdot B_\nu(t_{skin}) + (1 - \epsilon_\nu) \cdot \tilde{I}_\nu^\downarrow(\tau_\nu^*) + \alpha_\nu \cdot I_\nu^{\downarrow\odot}(\tau_\nu^*) ,$$ (2)

in which τ is the optical depth, and $\tau=0$ and τ_ν^* represents the top and the bottom of the atmosphere, respectively; μ is the cosine of the satellite viewing zenith angle; $B_\nu(t)$ is the Planck function for computing black-body radiation at temperature t;

150 $T_\nu(\tau)$ is the transmission at level τ; ϵ_ν is the emissivity; α_ν is the surface reflectance; $I_\nu^{\downarrow\odot}(\tau_\nu^*)$ is the solar radiation reaching the surface level; $\tilde{I}_\nu^\downarrow(\tau_\nu^*)$ is the total downwelling flux reaching the surface, integrated upon all the geometries by considering a Lambertian surface. Similar to **Clough et al. (2006)** and **Hurtmans et al. (2012)**, the evaluation of this equivalent downward flux integral can be simplified by computing an effective downward radiance with a zenithal angle of 53.51°, which gives a very accurate approximation of the integral for emissivity larger than 0.9 (**Turner, 2004**).

155 The monochromatic radiances at a high resolution of 0.05 cm⁻¹ (over-sampled by 12 times compared to GIIRS spectral resolution of 0.625 cm⁻¹) are simulated and then convolved with the GIIRS instrument line shape (ILS) to obtain calculated radiances at the same resolution as GIIRS that can directly be compared with the GIIRS spectra. ILS for GIIRS is constructed using a standard SINC function with a Maximum Optical Path Difference (MOPD) of 0.8 cm. The original spectra are not

apodized to retain the original spectral absorption features. Instead, a wide ILS, with a width of 40 cm^{-1}, is used to account for
160 the contribution from oscillating side lobes on both sides of the SINC function (**Gambacorta and Barnet, 2018**).

3.2 A priori atmospheric and surface parameters

The RT model in FY-GeoAIR requires inputs of atmospheric state parameters including profiles of temperature, water vapor,
and atmospheric composition and surface parameters. The data sources and their specifications are described below.

3.2.1 Model-derived CO climatology

165 Since CO is the primary gas to be retrieved, constructing an appropriate a priori for the retrieval algorithm is important. Similar
to the TES retrieval algorithms (**Luo et al., 2007**), we use a model-derived CO monthly climatology to create spatially and
temporally varying a priori CO fields. A climatology-based a priori provides the best a priori knowledge from the model and
was shown to have a better performance over regions with persisting high levels of CO throughout the year (**George et al.,
2015**). We used the CO simulations from the ECMWF CAMS global reanalysis (EAC4) monthly averaged fields (**Inness et
170 al., 2019**), which have a horizontal resolution of 0.75°×0.75°, a temporal resolution of 3-hour, and 25 pressure levels from
1000 hPa to 1hPa. We computed the 3-hourly CO profile climatology for each month using 5 years of simulations from 2017
to 2021.

3.2.2 Atmospheric profiles of H_2O, CO_2, N_2O, and O_3

In the spectral window from 2120 cm^{-1} to 2080 cm^{-1}, the interference gases include H_2O, CO_2, N_2O, and O_3. H_2O and O_3 are
175 extracted from ECMWF ERA5 reanalysis (**Hersbach et al., 2020**), which has a horizontal resolution of 0.25°×0.25°, a
temporal resolution of 1 hour, and 37 pressure levels from 1000hPa to 1hPa. N_2O and CO_2 are extracted from ECMWF CAMS
global inversion-optimized greenhouse gas fluxes and concentrations (**ECMWF, 2022**), which have a spatial resolution of
1.9°×3.75°, a temporal resolution is 3-hour, and 39 pressure levels from 1000hPa to 1hpa. The latest available year of datasets
in 2019 for N_2O and 2021 for CO_2 are used.

180 ### 3.2.3 Atmospheric temperature profile

The atmospheric temperature profile is a key input in the forward RT model for computing the blackbody emission by the
atmosphere. The atmospheric temperature data are extracted from ECMWF ERA5 reanalysis (**Hersbach et al., 2020**), which
has a horizontal resolution of 0.25°×0.25°, a temporal resolution of 1 hour, and 37 pressure levels from 1000hPa to 1hPa.

3.2.4 Surface emissivity, surface skin temperature, and surface pressure

185 Surface emissivity and skin temperature are important parameters in computing surface blackbody emission. For the surface
land data, we used the global infrared land surface emissivity database from the University of Wisconsin-Madison (UOW-M)
(**Seemann et al., 2007**). The dataset has 10 bands in wavenumber, ranging from mid-wave infrared to long-wave infrared.
Interpolation is performed to derive the emissivity in the CO channels. For ocean surface emissivity, we adopted the ocean
emissivity model, which is a function of viewing zenith angle and wind speed, from **Masuda et al. (1997)**. Surface skin

190 temperature and surface pressure are extracted from ERA5 hourly data on single level (**Hersbach et al., 2020**), which has a
spatial resolution of 0.25°×0.25°. The surface pressure from ECMWF reanalysis has a typical accuracy of 2–3hPa (**O'Dell et
al., 2012**).

The number of pressure grids in the forward RT model should be large enough to reduce the error associated with the
discretization of the atmosphere. Here we define a 47 layers target atmosphere with an equal thickness of about 1 km from

195 1000 hPa to 1hPa. All the above-described atmospheric a priori profiles are interpolated to the target pressure grids. The
pressure grids are kept fixed except for the surface level which is determined by the surface pressure.

3.3 Spectroscopic database: Look-up tables of absorption cross-section

Deriving the absorption optical depth of gas molecules for the RT model would require the line-by-line calculation of
absorption cross section based on spectroscopic line parameters and line shape. However, this line-by-line calculation at high

200 spectral resolution for a wide spectral window is computationally expensive. Instead, to speed up the calculation, absorption
coefficient (ABSCO) for different molecules at different pressures and temperatures are precalculated and stored in lookup
tables (LUTs). For gas absorptions that have H_2O dependence, the ABSCO dependence on H_2O is also considered. This
method of building ABSCO lookup tables has been adopted in previous retrieval algorithms, including the FORLI for IASI
(**Hurtman et al., 2012**) and the ELANOR for TES (**Clough et al., 2016**).

205 In this study, ABSCO LUTs are built using the extensively validated Line-By-Line Radiative Transfer Model (LBLRTM
v12.11; **Clough et al., 2005**). LBLRTM uses the HITRAN database as the basis for line parameters. These line parameters
from HITRAN, plus additional line parameters from other sources, are combined for LBLRTM by a line file creation
program called LNFL (v3.2). In addition to modeling individual spectral lines and absorption cross-sections, LBLRTM also
takes into account the H_2O, CO_2, O_2, and N_2 continua in the thermal infrared using the MT_CKD continuum database

210 (MT_CKD_3.4). The self-broadening absorption of H_2O nonlinearly depends on its concentration which should be
considered for calculating H_2O ABSCO. It has been shown that the dependence is nearly linear for a given temperature and
pressure. Therefore, to account for this effect in the LUT, we computed the H_2O ABSCO at two H_2O volume mixing ratio
(VMR) values: 1ppm (dry air) and 4×10^4 ppm (wet air). The ABSCO values at other H_2O values can be calculated by linear
interpolation. In LBLRTM, the line-by-line calculation resolution is set to be 2.0×10^{-4} cm^{-1} and later integrated into the

215 ABSCO LUT table resolution at 5.12×10^{-2} cm^{-1}, which is oversampled by about 10 times compared to the GIIRS resolution

of 0.625 cm^{-1}. The LUTs are built for 49 atmospheric pressure levels from 1025 hPa to 1 hPa with a pressure step equivalent to 1 km, and 15 temperatures from 180 to 320 K with a step of 10K.

4 Retrieval algorithm in FY-GeoAIR based on optimal estimation theory

The goal of the retrieval algorithm for retrieving CO from nadir-viewing instruments based on optimal estimation theory is
220 to find a solution for the state vector, which consists of CO profile and auxiliary parameters, such that the RT simulations best fit the measured spectra. The optimal estimation method has been described thoroughly in **Rodgers (2000)** and applied in several previous studies by the group (**Zeng et al., 2017; Zeng et al., 2021; Natraj et al., 2022**).

4.1 Atmospheric inversion based on optimal estimation

The general forward model that relates the state vector (x) to the measurement vector (y) is given by:

225 $$y = \mathbf{F}(x, b) + \varepsilon,\qquad(3)$$

where y is the observed GIIRS spectral radiance at the CO retrieval window from 2143 cm^{-1} to 2181.25 cm^{-1}, which is found to be the best window that minimizes interferences by other gases while maximizing the information content for CO retrieval (**De Wachter et al., 2012**); x is the state vector consisting a set of parameters to be retrieved, including CO profile, H_2O profile, surface skin temperature and atmospheric temperature profiles. $\mathbf{F}$ is the forward RT model for simulating radiance as
230 introduced in **Sect. 3**; b is a set of model parameters in the RT model that are not retrieved, such as profiles of interference gases (O_3, CO_2, and N_2O), surface emissivity, and other relevant geophysical parameters. ε is the spectral error vector containing the noise in the spectra observation. The goal of optimal estimation is to find the solution for the state vector that minimizes the following cost function (**Rodgers, 2000**):

$$J(x) = \chi^2 = [y - \mathbf{F}(x, b)]^T S_\varepsilon^{-1} [y - \mathbf{F}(x, b)] + (x - x_a)^T S_a^{-1}(x - x_a),\qquad(4)$$

235 where S_ε is the measurement error covariance matrix; x_a is the *a priori* state vector; S_a is the *a priori* covariance matrix for the state vector. For simplicity in calculating S_ε, we assume that the measurement noise dominates and there is no cross-correlation between different spectral channels, resulting in a diagonal matrix. The instrument noise (NedR) for each spectral observation, as described in **Sect. 2.2**, is used as the measurement noise. A commonly used statistic for quantifying the goodness of fit is the reduced χ^2, which is computed as the cost function value after convergence divided by the degree of
240 freedom, which is the number of channels in the absorption window (which is 64) minus the number of elements in the state vector (which is 4). After evaluating the reduced χ^2 from test runs, we found that the value on average is systematically lower than the theoretical mean value of 1.0, indicating that the measurement error has been underestimated. Therefore, in this study, we enlarge the measurement noise by 1.5 times such that the averaged reduced χ^2 value from the retrievals is close to 1.0. The extra noise added may represent the uncertainty from the forward model, spectroscopy, and the forward model inputs, which

245   are not accounted for by the original instrument noise alone. $\mathbf{S}_a$ is a very important parameter that should not be too tight or loose to provide suitable constrain on the retrieval. It can be calculated based on the error in CO a priori profile and the correlation matrix derived from model simulations. In this study, the error in the CO profile is set to be 30%, following **Deeter et al. (2010)** for MOPITT, which we found to be close to the error estimate (one standard deviation) in the CAMS CO simulations; To construct the correlation matrix, we used a correlation length of 3 km based on our analysis using CAMS CO

250   simulations.

     To obtain the solution for **Equation (4)**, we adopt the Levenberg-Marquardt method (**Rodgers, 2000**) to find the optimal estimate of $\boldsymbol{x}$ that minimizes the cost function through an iterative process:

$$\boldsymbol{x}_{i+1} = \boldsymbol{x}_i + [(1+\gamma)\mathbf{S}_a^{-1} + \mathbf{K}_i^T\mathbf{S}_\varepsilon^{-1}\mathbf{K}_i]^{-1}\{\mathbf{K}_i^T\mathbf{S}_\varepsilon^{-1}[\boldsymbol{y} - \mathbf{F}(\boldsymbol{x}_i,\boldsymbol{b})] - \mathbf{S}_a^{-1}[\boldsymbol{x}_i - \boldsymbol{x}_a]\}, \tag{5}$$

where the subscript i indicates the ith iteration; The parameter γ is chosen at each iteration to minimize the cost function. The

255   strategy to choose γ is described in **Rodgers (2000)**. $\mathbf{K}$ is the Jacobian matrix, which is the first derivative of the forward model with respect to the state vector:

$$\mathbf{K}_i = \partial\mathbf{F}(\boldsymbol{x}_i,\boldsymbol{b})/\partial\boldsymbol{x}_i, \tag{6}$$

where each element in $\mathbf{K}_i$ quantifies the sensitivity of the simulated radiance to the corresponding geophysical variable in the state vector. Although analytical expression can also be derived, we used the finite difference to compute $\mathbf{K}$ for its simplicity.

260   At convergence, the *a posteriori* error matrix $\hat{\mathbf{S}}$ can be estimated by:

$$\hat{\mathbf{S}} = (\mathbf{K}^T\mathbf{S}_\varepsilon^{-1}\mathbf{K} + \mathbf{S}_a^{-1})^{-1}, \tag{7}$$

4.2 Averaging kernel matrix and Degree of Freedom for Signal (DOFS)

The quality of the retrieval can be characterized by two quantities: the AK matrix and the DOFS. AK matrix is an important statistical metric for describing the sensitivity of the retrieval to the true state by the current observing system. The full

265   averaging kernel matrix ($m \times m$) is given by:

$$\mathbf{A} = (\mathbf{K}^T\mathbf{S}_\varepsilon^{-1}\mathbf{K} + \mathbf{S}_a^{-1})^{-1}\mathbf{K}^T\mathbf{S}_\varepsilon^{-1}\mathbf{K}, \tag{8}$$

where m is the number of atmospheric layers. A_{ij} represents the derivative of the retrieved CO at level i with respect to the true CO at level j, representing a relative contribution of the true state to the retrieved state. An ideal observing system would produce an AK matrix close to the identity matrix, meaning the observations are sufficiently good to constrain each element

270   in the retrieval vector. In reality, the AK can be very different from an identity matrix, meaning that the information from the true state is smoothed vertically over different layers by the retrieval algorithm. The rows of AK can be regarded as smoothing functions. The trace of the AK matrix, representing the number of independent elements of information extracted by the retrieval algorithm from the measurement, quantifies the DOFS. It is an important concept in describing the vertical resolution

of the retrieval profile. For example, a DOFS of 1 means that at least one independent piece of information on the vertical
275 distribution of CO can be retrieved from the spectral measurement.

4.3 Post-processing

All cloud-screened GIIRS spectra acquired over land and ocean at solar zenith angle less than 70° are used in the retrieval. In
the post-processing, multiple filters are applied to ensure good retrieval quality. First, retrievals that fail to converge after 15
iterations are excluded. Second, retrievals with the goodness of fit, quantified by reduced χ^2, less than 1.5 are excluded. Lastly,
280 outliers of the CO total column defined as values that are more than 3 standard deviations away from the mean are excluded.

5 Inversion experiments using simulated synthetic spectra

The goal of applying the FY-GeoAIR algorithm to simulated synthetic spectra is to assess the performance of the algorithm in
retrieving CO profiles and to quantify the impacts on the accuracy due to the spatially and temporally varying thermal contrast
(TC) in East Asia. TC is defined as the temperature difference between the surface and the lower atmospheric layer (**Clarisse**
285 **et al., 2010**), and is found to be a key indicator of the information content for retrieving CO profile, especially the lower
tropospheric CO, from infrared thermal radiance.

The synthetic spectra are generated using the same forward RT model as described in **Sect. 3**, except that we use the original
ECMWF EAC4 3-hourly simulated CO as the "truth" and add Gaussian white noise with a standard deviation equal to
NedR×1.5. The retrieval algorithm is then applied to these synthetic spectra using a priori CO from monthly climatology as
290 described in **Sect. 3.2**. Since we assume no error in the forward RT model, the spectra error in the retrieval algorithm solely
comes from the added noise. The retrievals are finally compared with the "truth" to investigate the impacts of TC and AK on
their differences.

Three representative regions are specially selected for inter-comparisons, including (1) North China Plain (covering 30°-
40°N and 110°-120°E), which represents industrialized urban regions with persistently high CO emissions; (2) Mongolia
295 (covering 40°-50°N and 100°-115°E), which represents CO background regions; and (3) the East China Sea (covering 25°-
35°N and 122°-130°E), which represents ocean surface. As shown in **Fig. 2**, the diurnal changes of surface temperatures and
bottom air temperatures show distinctive patterns over these three regions. Compared to the atmosphere, Earth's surface,
especially over land, heats up and cools down more quickly because of its relatively low heat capacity. This mechanism results
in a larger diurnal variation for the surface than for the atmosphere: TC is thus more pronounced during the day than the night.
300 Specifically, the East China Sea has a relatively flat change, as expected for ocean water due to its large heat capacity and
ocean water mixing; The Mongolia region, covered by a mixture of grass and bare land, has the largest diurnal change; The
North China Plain, surrounded by urban clusters with a mixture of residential and agriculture lands, has a moderate diurnal

change. The complexity of the diurnal TC change as demonstrated by various land use types in East Asia has a significant

impact on the uncertainty of CO retrievals from GIIRS.

305
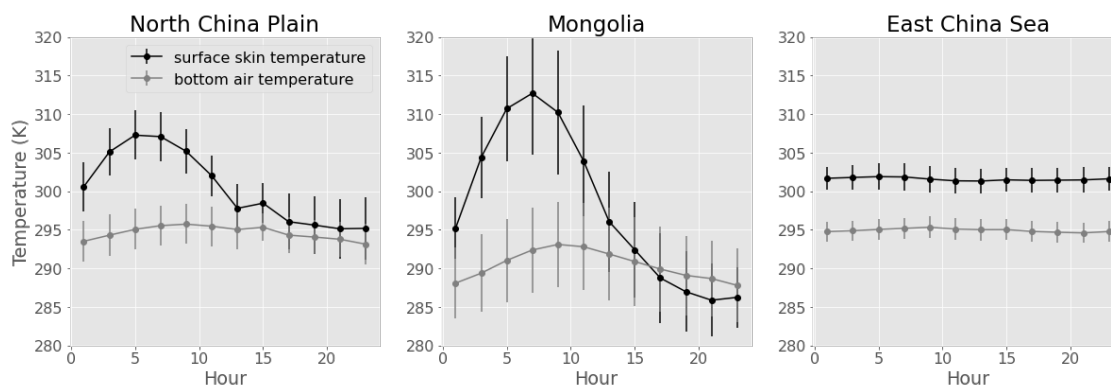
Figure 2: The diurnal change of surface temperature and bottom layer air temperature extracted from ECMWF ERA5 reanalysis data for the three representative regions: North China Plain, Mongolia, and the East China Sea. These temperature values are averaged for every two-hour corresponding to the clear-sky GIIRS observations in July 2022.

As shown in **Fig. 3 (a)** by taking North China Plain as an example, TC is significantly correlated with the DOFS from the

CO retrievals for both the total column and the bottom 0-1 km layer partial column. A similar relationship can be found in

LEO satellites (e.g., **Bauduin et al., 2017**). In addition, a higher DOFS leads to a smaller bias in the retrieval CO total columns,

310 as shown in **Fig. 3(b)**. A similar pattern can be seen for the bottom layer CO partial columns, but slightly less obvious. A

possible explanation is that, when the DOFS is small, the information for the bottom layer CO may be extrapolated from the

free troposphere (**Bauduin et al., 2017; George et al., 2015**). This information extrapolation may lead to a higher bias in the

retrieval for the bottom layer CO, as can be seen from **Fig. 3(b)** when DOFS is small. Overall, we can conclude that a higher

(lower) TC leads to a higher (lower) DOFS for the retrieval, which in turn contributes to a smaller (larger) bias in the retrieval.

315 To evaluate the performance of the retrieval algorithm, we compare (1) the retrievals and the "truth" and (2) the retrievals

and the a priori in North China Plain, Mongolia, and the East China Sea, respectively. From **Fig. 4**, we can see that the retrieved

CO total columns have a higher correlation with the "truth" than with the a priori, suggesting that the retrieval algorithm are

effective and the observed spectra are providing useful information to constrain the CO profiles. Since the sensitivity of the

CO retrieval is pressure dependent, we implement a profile correction by applying the GIIRS AK to smooth the "truth" profile,

320 to account for the different resolution between the retrieval and the "truth" (**Rodgers and Connor, 2003**):

$$x_{true}^{AKcorrect} = x_a + \boldsymbol{A} \cdot (x_{true} - x_a) , \qquad (9)$$

where $x_{true}^{AKcorrect}$ is the smoothed "truth" profile and x_a and $\boldsymbol{A}$ are the a priori profile and AK matrix, respectively, from the

GIIRS retrieval. The result is shown in the 3rd column in **Fig. 4**. The correlations are significantly improved, justifying the use

of AK matrix smoothing for the CO profile from model simulations that have uniform vertical sensitivity. For example, if the

325 model simulation data are close to the "truth", then after the AK matrix smoothing, the corrected data should be in high agreement with our GIIRS retrievals. However, for comparison with CO retrievals that have different a priori profiles and AK matrix, a different correction method needs to be implemented and is introduced in **Sect. 6.4**.
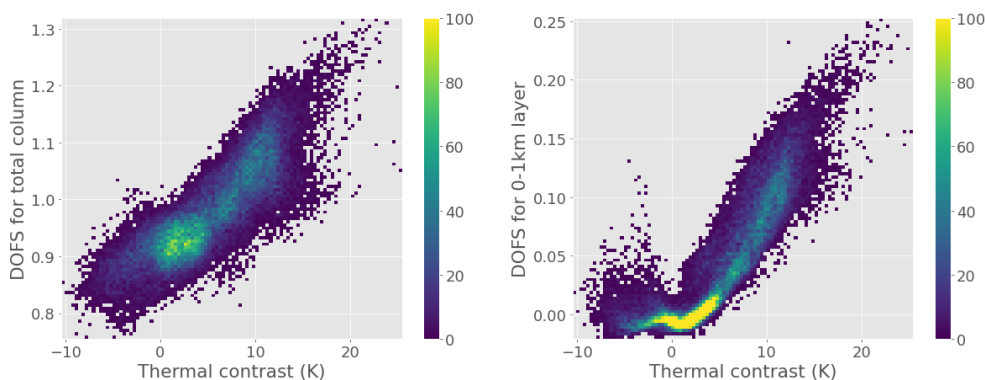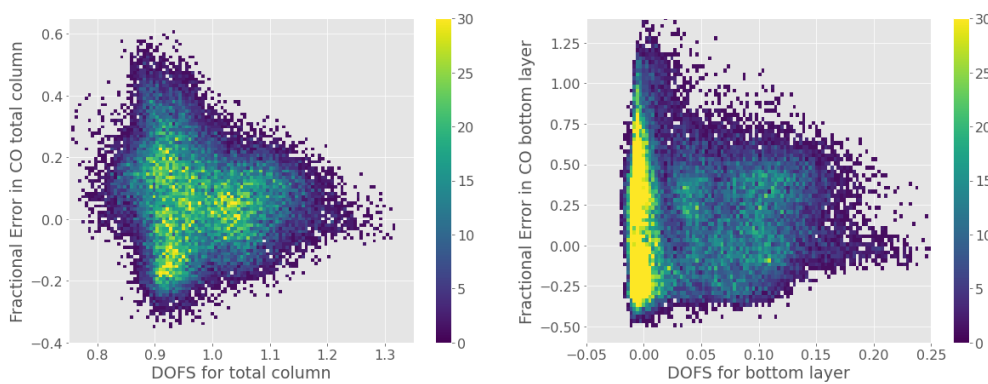
Figure 3: (a) DOFS as a function of TC for CO total column (left) and bottom 0-1km layer CO partial column (right) in North China Plain; (b) Fractional retrieval error derived by the difference between the retrieval and the "truth" as a function of DOFS for CO total column (left) and bottom layer CO partial column (right) in North China Plain. The color bar indicates the number of data points.

330

335

340
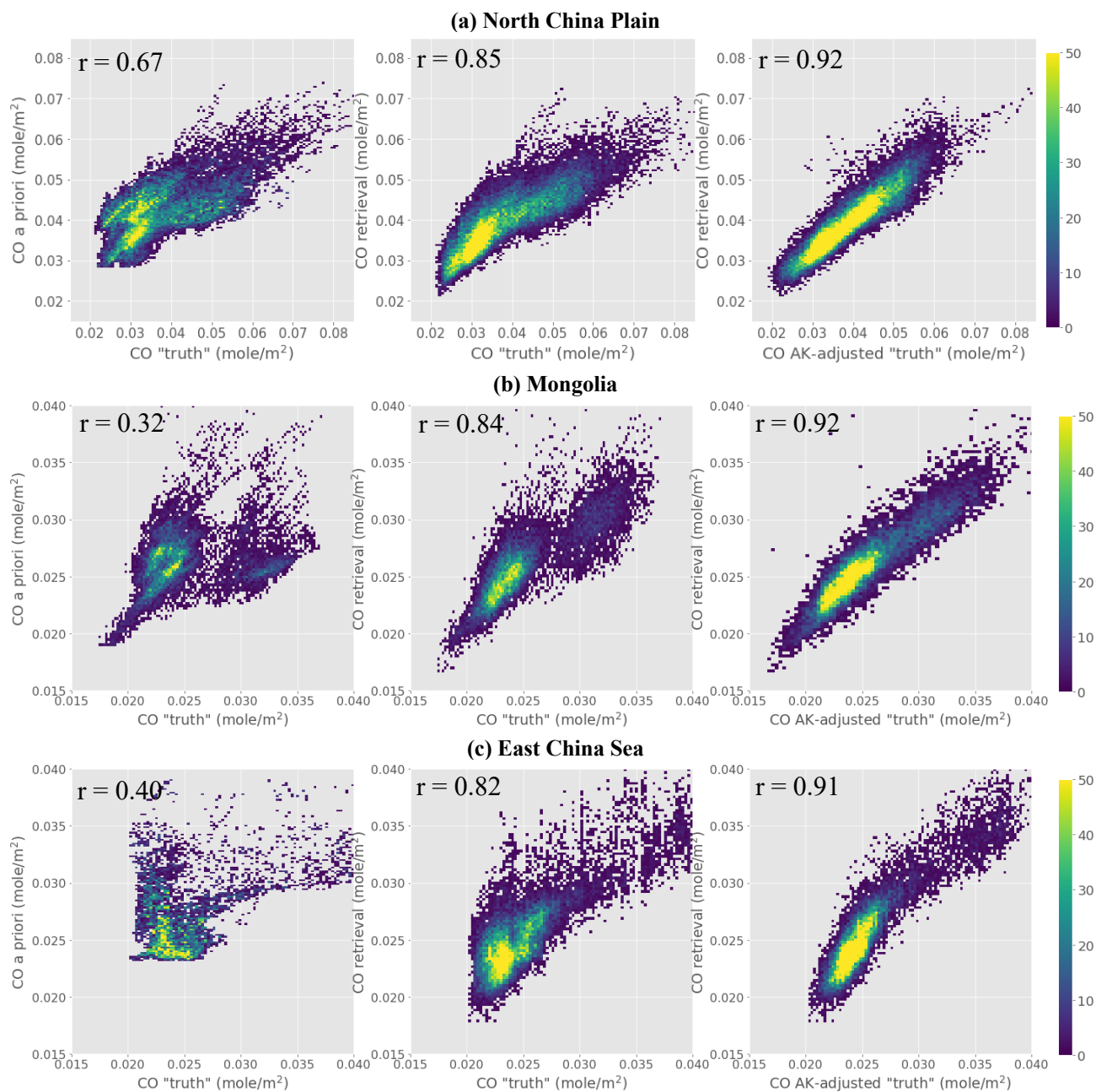
Figure 4: Retrieval result of CO total column from synthetic spectra for the three representative regions: (a) North China Plain, (b) Mongolia, and (c) the East China Sea. The first column compares CO a priori CO column with the "truth", the second column compares the retrieved CO column with the "truth", and the third column compares the retrieved CO column with the "truth" that has been smoothed by the GIIRS AK matrix. The color bar indicates the number of data points.

6. Characteristics of CO retrievals from GIIRS

345
All cloud-screened GIIRS spectra acquired over land and ocean at solar zenith angle less than 70° are used in the FY-GeoAIR retrieval algorithm. The retrieval results have been post-screened by the filters described in **Sect. 4.3**. In this section, we describe the characteristics of the CO retrievals, including the goodness of spectral fitting, DOFS and vertical sensitivity using AK matrix, and accuracy assessment by comparison with IASI CO retrievals.

(a)
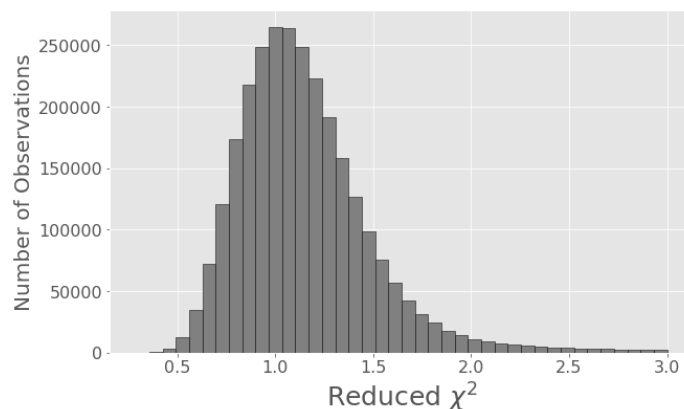
(b)
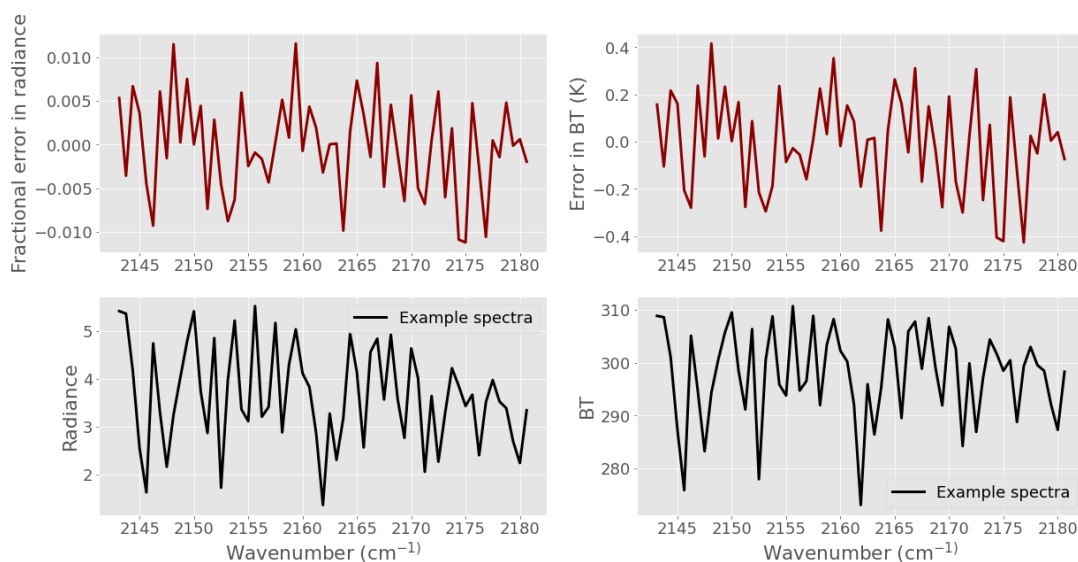
Figure 5: Statistics from spectral fitting. (a) The histogram of reduced χ^2 for spectral fitting from all retrievals using GIIRS spectra; (b) The upper panel shows the spectral fitting residual in the fractional error of radiance (left) and in BT (right) averaged over post-screened retrievals in hours 0-2 UTC. The results for the remaining observation hours are very similar and therefore not shown here. The lower panel shows examples of the observed spectra in the retrieval window in radiance (left) and BT (right). The standard deviations of fitting errors are very consistent across different channels, which are 0.017 for the fractional error in radiance and 0.6 K for the BT error.

6.1 Statistics for spectral fitting

The goodness of spectral fitting is evaluated by two statistics: the spectral fitting residual and the reduced χ^2. The latter
350 measures how large is the spectral fitting residual compared to spectral noise. The histogram of the reduced χ^2 and the
averaged fitting residuals for all the retrievals in July 2022 are shown in **Fig. 5**. The reduced χ^2 shows an expected distribution
centering around 1.0. In the post-processing step, we filter the values that are larger than 1.5. The choice of the threshold may
vary, here we chose 1.5 to retain more good quality data while removing retrievals that have an unsatisfactory fitting. The
spectral fitting errors in radiance and brightness temperature (BT) show no significant bias. Although a systematic pattern, that
355 is persistent among observations at different hours, can be seen from the averaged fitting residual from all spectra. However,
this pattern is not correlated with the absorption feature of the target gas CO or the primary interference gas H_2O (**Fig. 1(c)**).
This suggests that the CO spectroscopy adopted from LBLRTM which has undergone extensive verifications is accurate for
the purpose of this study. The standard deviations of fitting errors are very consistent across different channels, which are
0.017 for the fractional error in radiance and 0.6 K for the BT error. The latter suggests that the majority of the channels have
360 fitting errors of less than 1K. This result is consistent with the pre-launch assessment as described in **Sect. 2.2** and Li et al.
(2022).

6.2 Information content analysis

The information content of GIIRS observations is assessed by using the AK matrix and DOFS. The AK matrix represents the
sensitivity of the retrieved state to the true state, in which the matrix row represents how a specific retrieved state vector
365 element reacts to true changes of the state vector at different layers. In the case of the CO profile, for each retrieved layer, the
AK peak at the altitude containing most information about the profile. The AK thus provides an estimation of the altitude of
maximum sensitivity. **Fig. 6** shows examples of AK rows from two different scenarios of TC: higher TC in the daytime
(TC=11.3K) and low TC in the nighttime (TC=-2.7K). The distinctive difference in the lower tropospheric AK values
demonstrates the importance of high TC in providing information to the lower tropospheric CO retrievals. For the low TC
370 scenario, little information is available from the lower troposphere and the altitude with maximum sensitivity is located around
400 hPa (~6km). In such a case, the information for CO in the lower troposphere is thus extrapolated from the mid-troposphere,
which may lead to high bias for the lower troposphere estimate. **Fig. 7** shows that the diurnal (every 2-hour) change of AK
diagonal elements in North China Plain, Mongolia, and the East China Sea averaged over all days in July of 2022. The diurnal
changes are primarily driven by the changes in TC as shown in **Sect. 5**. As the TC increases and peaks in the afternoon, the
375 AK diagonal value increases, and the layer with the maximum moves closer to the surface. In contrast, the East China Sea
region has little change among different hours because the TC is relatively flat throughout the day. These results demonstrate
that the TC is significantly correlated with the vertical structure of AK rows from GIIRS retrievals.
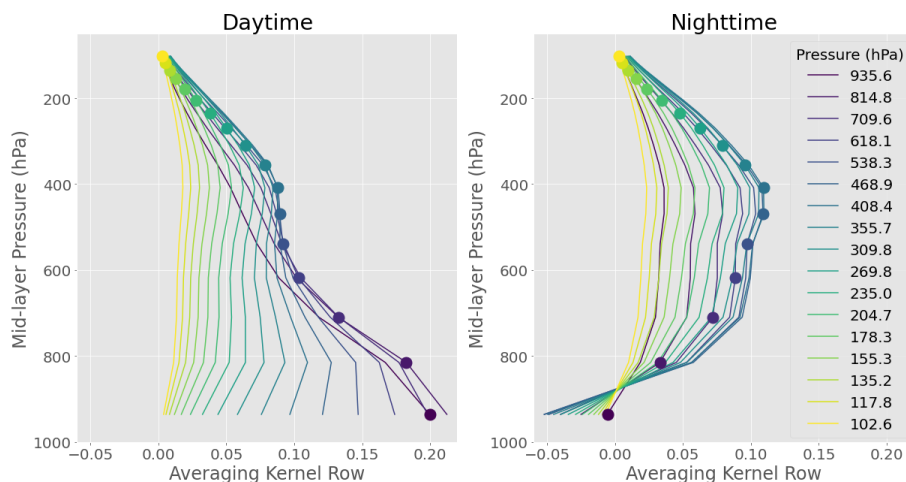
Figure 6: Examples of averaging kernel rows from two different scenarios of TC: (left) high thermal contrast in the daytime (TC=11.3K) and (right) low thermal contrast around Beijing in the nighttime (TC=-2.7K).

380
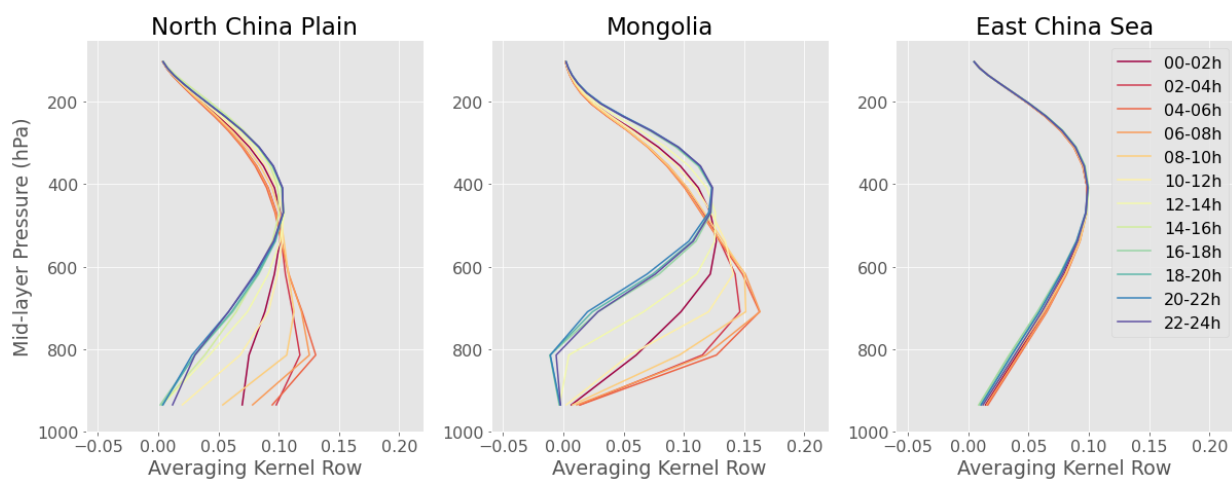
Figure 7: Diurnal (every 2-hour) change of averaging kernel diagonal elements in North China Plain (left), Mongolia (center), and East China sea (right) averaged over all days in July of 2022.
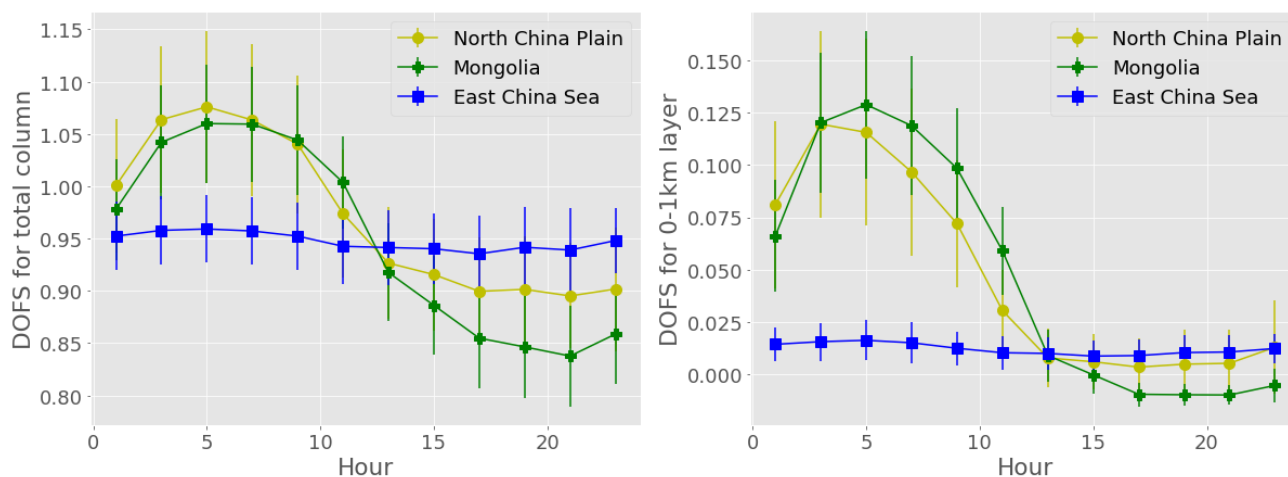
Figure 8: The diurnal changes of the DOFS mean and standard deviations for (left) CO total column and (right) the bottom 0-1km layer partial column in the three representative regions: North China Plain, Mongolia, and the East China Sea. These data are averaged over all days in July 2022.

385   DOFS represents another important metric for information content from GIIRS spectra. It quantifies the number of independent information available from the measurement. **Fig. 8** shows the diurnal changes of the DOFS mean and standard deviation in the three representative regions averaged over all days in July of 2022. In general, the diurnal changes of DOFS track the TC changes over these regions (**Fig. 2**). Interestingly, we see that the North China Plain has comparable DOFS to Mongolia, although the latter has a significantly larger TC. This is because, besides TC, the high CO concentration in North

390   China Plain has a positive contribution to the DOFS, as suggested by **Bauduin et al. (2017)**.

To investigate the relationship between TC and DOFS, the DOFS from the retrievals as a function of TC for the CO total column and bottom 0-1km layer CO partial column for the three representative regions are plotted in **Fig. 9**. While the DOFS for the CO total column shows a monotonic change with TC, the DOFS for the 0-1km shows a bowl-shape, with DOFS increases as the TC becomes more negative. This pattern is consistent with findings by **Bauduin et al. (2017)**, which showed

395   that large negative TC values allow the decorrelation between the low and the high troposphere by capturing the emission of radiation from the lower troposphere. Overall, the DOFS for the total CO column retrieval is between 0.6 and 1.2 for the majority, with a mean value around 1.0, meaning that about one independent piece of information is retrieved from GIIRS spectra. The highest DOFS exists over the land region with the largest TC. Similarly, for the DOFS for the bottom 0-1km layer, increasing the TC value favors the sensitivity to surface CO. The DOFS can be as large as 0.3, providing strong constrain on

400   the bottom 0-1 km CO. The value in the North China Plain is generally larger than Mongolia and the East China Sea even for the same TC. This is because the persistently high CO concentration in North China Plain is another important contributor to the total DOFS besides TC (**Bauduin et al., 2017**).

(a) North China Plain
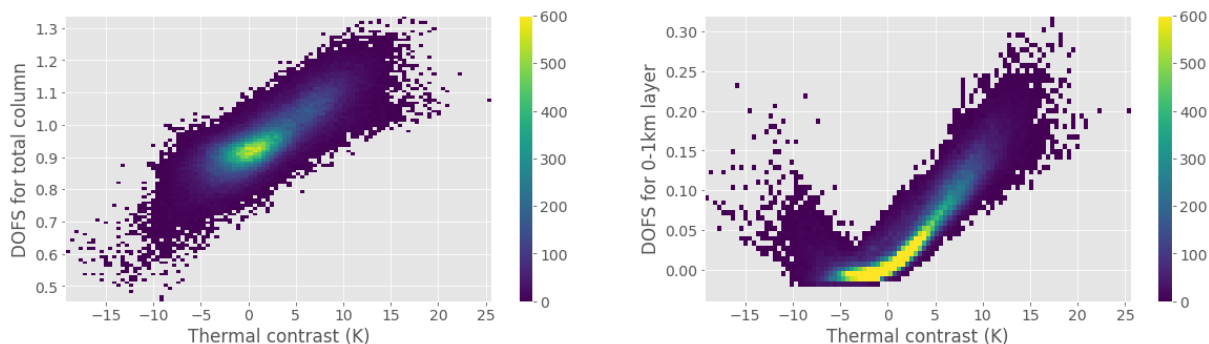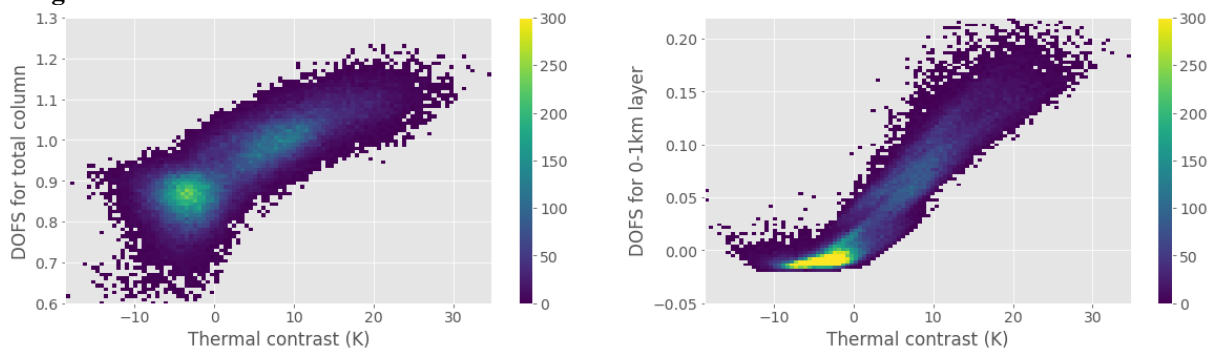
(b) Mongolia

(c) East China Sea
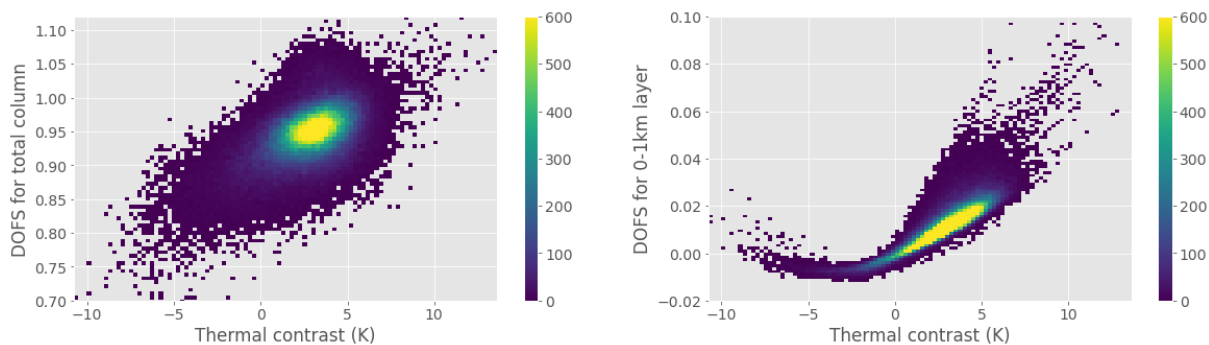
Figure 9: DOFS from the retrievals as a function of TC for CO total column (left) and bottom 0-1km layer CO partial column (right) for the three representative regions: (a) North China Plain, (b) Mongolia, and (c) the East China Sea.

405
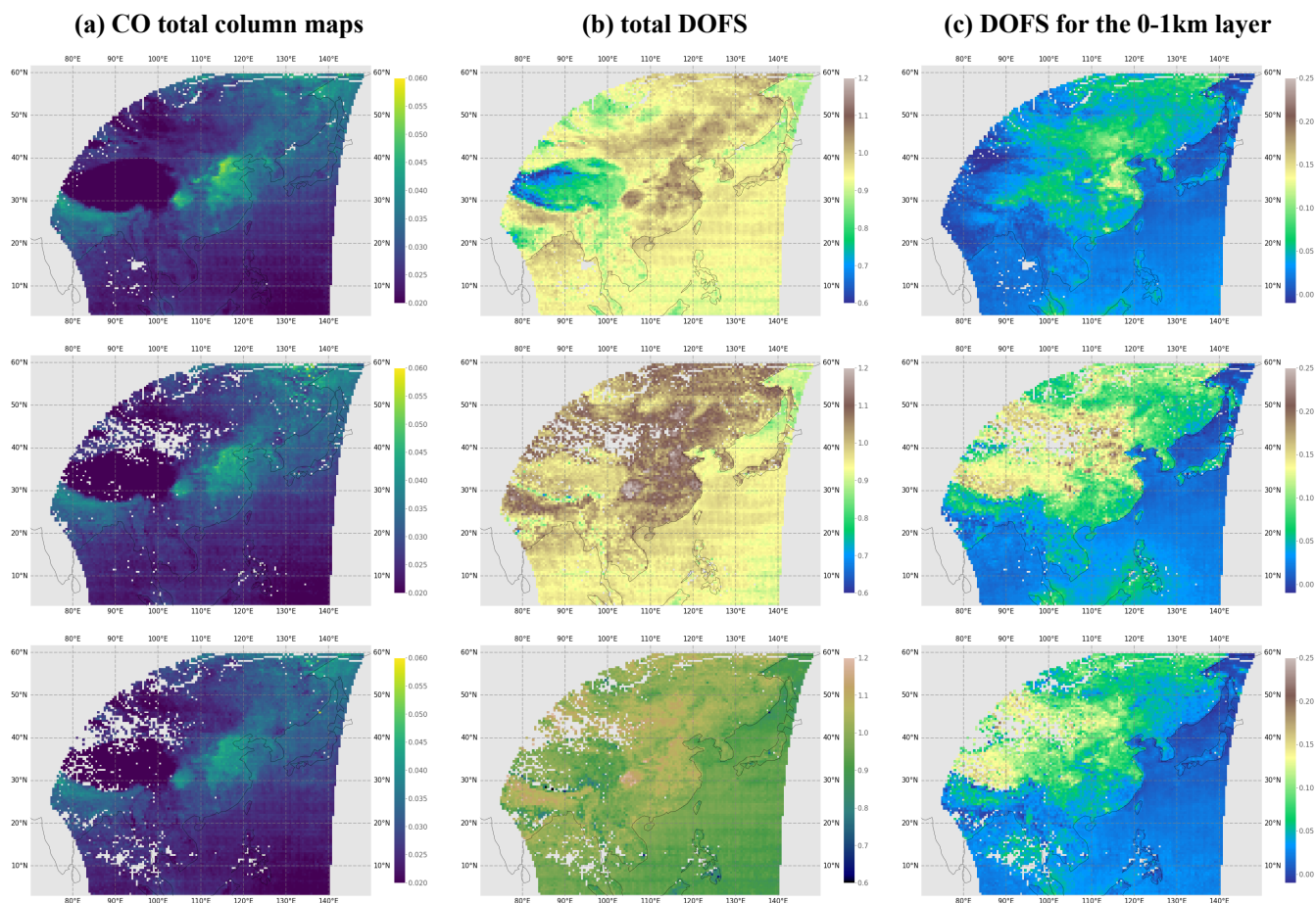
Figure 10: (a) Maps of retrieved CO total columns from GIIRS for hours 0-2, 4-6, and 8-10 UTC. The CO total columns are monthly averages in July of 2022 in 0.5°×0.5° grids; (b) The distribution of DOFS for the CO total column; and (c) The distribution of DOFS for the CO parital column at the bottom 0-1km layer.

(a) CO total column maps **(b) total DOFS** **(c) DOFS for the 0-1km layer**
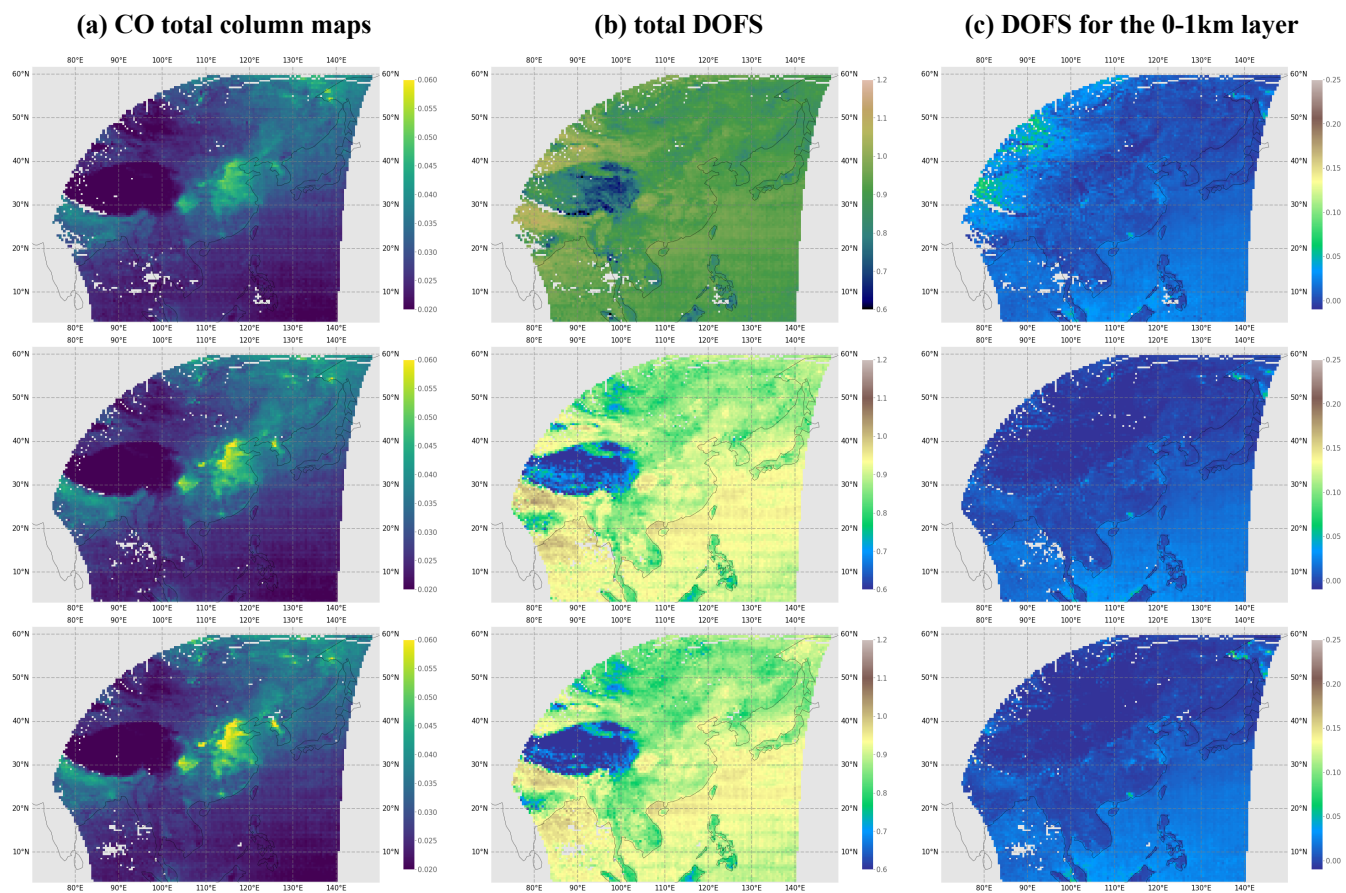
Figure 11: The same as Fig. 10 but for hours 12-14, 16-18, and 20-22 UTC.

410

6.3 Spatial distribution of CO total column and the DOFS from retrieval

The CO total column and the DOFS from the retrieval algorithm are averaged for every scan of East Asia (2-hour duration) by aggregating the data from all days in July 2022 into $0.5° \times 0.5°$ grids. The goal is to compare the diurnal changes of the spatial distribution of (1) the retrievals and (2) the DOFS values for both the total column and the bottom 0-1km layer partial

415   column. The results are shown in **Fig. 10(a)** and **Fig. 11(a)** for the CO total column retrievals. In total, 12 full domain measurement cycles in East Asia are available for every 2 hours. Here, we only show every other scan as examples, in total 6 full domain measurements for hours 0-2h, 4-6h, 8-10h, 12-14h, 16-18h, and 20-22h UTC. Overall, the spatial distribution of the CO total column shows expected spatial patterns, with high values clustered in industrialized urban regions in northern and eastern China, the Sichuan basin in central China, and northern India. Although the CO changes in a day but the spatial pattern

420   is very persistent.

To evaluate the information content that is available in constraining the CO total column and the bottom 0-1km layer partial column, the maps of the DOFSs are also shown in **Fig. 10(b)(c)** and **Fig. 11(b)(c)**. In the daytime, when TC is high, the DOFS values over land, especially over easter and northern China, are higher than 1.0, suggesting that the GIIRS spectra provide more than 1 piece of independent information to the retrieval. In the nighttime, when the land region cools down quickly and

425   the ocean surface is still warm, a larger TC over the ocean leads to a higher DOFS compared to the land region. A similar pattern can be observed in the DOFS for the bottom 0-1 km layer, but with smaller DOFS values. Not surprisingly, the DOFS for the bottom 0-1km layer also shows a local pattern as the CO emissions (e.g., in northern China). This is because the DOFS from the retrieval is also affected by the CO concentration besides TC, as discussed in **Section 6.2** and **Bauduin et al. (2017)**.

6.4 Accuracy assessment by comparison with IASI CO retrievals

430   Different from FY-4B/GIIRS, IASI onboard Metop-B, which was launched in 2012, is a sun-synchronous polar-orbiting infrared spectrometer designed to measure the upwelling spectral radiance in the infrared using a nadir viewing geometry, with equator crossing times at 10:30 am and 10:30 pm LT, respectively, in the morning and evening. IASI has a dedicated CO retrieval algorithm (**Hurtmans et al., 2012**) that was improved over time and has benefited from cross-comparisons with other products (e.g., **George et al., 2009; Wachter et al., 2012; Worden et al., 2013; George et al., 2015**). Therefore, a comparison

435   would shed light on the difference between GIIRS infrared CO retrievals and the state-of-the-art retrievals from IASI. In this section, we carry out the comparison using publicly available CO from IASI/Metop-B.

Because the GIIRS and IASI have a different footprints and grid configurations, it is not straightforward to make a point-by-point comparison. Instead, we focus on the three representative regions (North China Plain, Mongolia, and the East China Sea) and compare the regionally averaged CO total columns between GIIRS and IASI. Two kinds of comparisons are carried

440   out: (1) a direct comparison of daily changes between the CO total columns; (2) comparing the CO total columns after considering their differences in the a priori and AK in the retrievals. Since GIIRS and IASI retrievals have different a priori and AK, a direct comparison may not be appropriate (**Luo et al., 2007**). Following **Rodgers and Connor (2003)**, we

implement a data correction, including an a priori adjustment and an AK smoothing, to account for the difference in a priori and AK, respectively, between IASI and GIIRS retrievals. In step 1, we adjust the GIIRS retrievals to the IASI a priori, given

445 by:

$$x_{adj}^{GIIRS} = x_{ret}^{GIIRS} + (A^{GIIRS} - I)(x_a^{GIIRS} - x_a^{IASI}) \,, \tag{10}$$

Since the IASI FORLI algorithm uses a fixed a priori profile, this adjustment can be easily implemented. In step 2, we smooth the IASI retrievals using the GIIRS AK matrix, given by:

$$x_{smooth}^{IASI} = A^{GIIRS} x_{ret}^{IASI} + (I - A^{GIIRS}) x_a^{IASI} \,, \tag{11}$$

450 since GIIRS and IASI have different footprint sizes and spatial resolutions, for every IASI retrieval, the closest GIIRS AK matrix is used. After the correction, we average the data for all the days in July 2022. The results of daily means are shown in **Fig. 12** for North China Plain, Mongolia, and the East China Sea.

The direct comparison between GIIRS and IASI shows good agreement, with all correlation coefficients larger than 0.7 for the three representative regions. Specifically, the daily variabilities are highly consistent between the two datasets. Since

455 in their retrieval algorithms the a priori CO total columns used in GIIRS and IASI do not vary with days, the daily changes of the retrieved CO total columns directly reflect the available information in the observations from both instruments. Given that the GIIRS and IASI are two different instruments and that the former uses spatially and temporally varying CO climatology while the latter uses a fixed profile as the a priori, this consistency between GIIRS and the state-of-the-art IASI CO retrievals demonstrate the effectiveness of FY-GeoAIR algorithm in constraining CO profiles from GIIRS. After

460 correction using a priori adjustment and AK smoothing, their consistencies generally improve. In the North China Plain, the difference in nighttime measurements is significantly reduced. The large decreases in both their absolute CO columns after correction are related to, in the lower troposphere, the smaller IASI a priori compared to GIIRS and the lower GIIRS AK values compared to IASI. In the Mongolia region, no significant changes can be seen mainly because over this background region the a priori and AK values are close between IASI and GIIRS. However, systematic bias can be seen in the East

465 China Sea. After the correction, the bias is reduced and the correlation coefficients have been improved, although a small bias remains, suggesting this correction may not be as effective over ocean surface as over land.
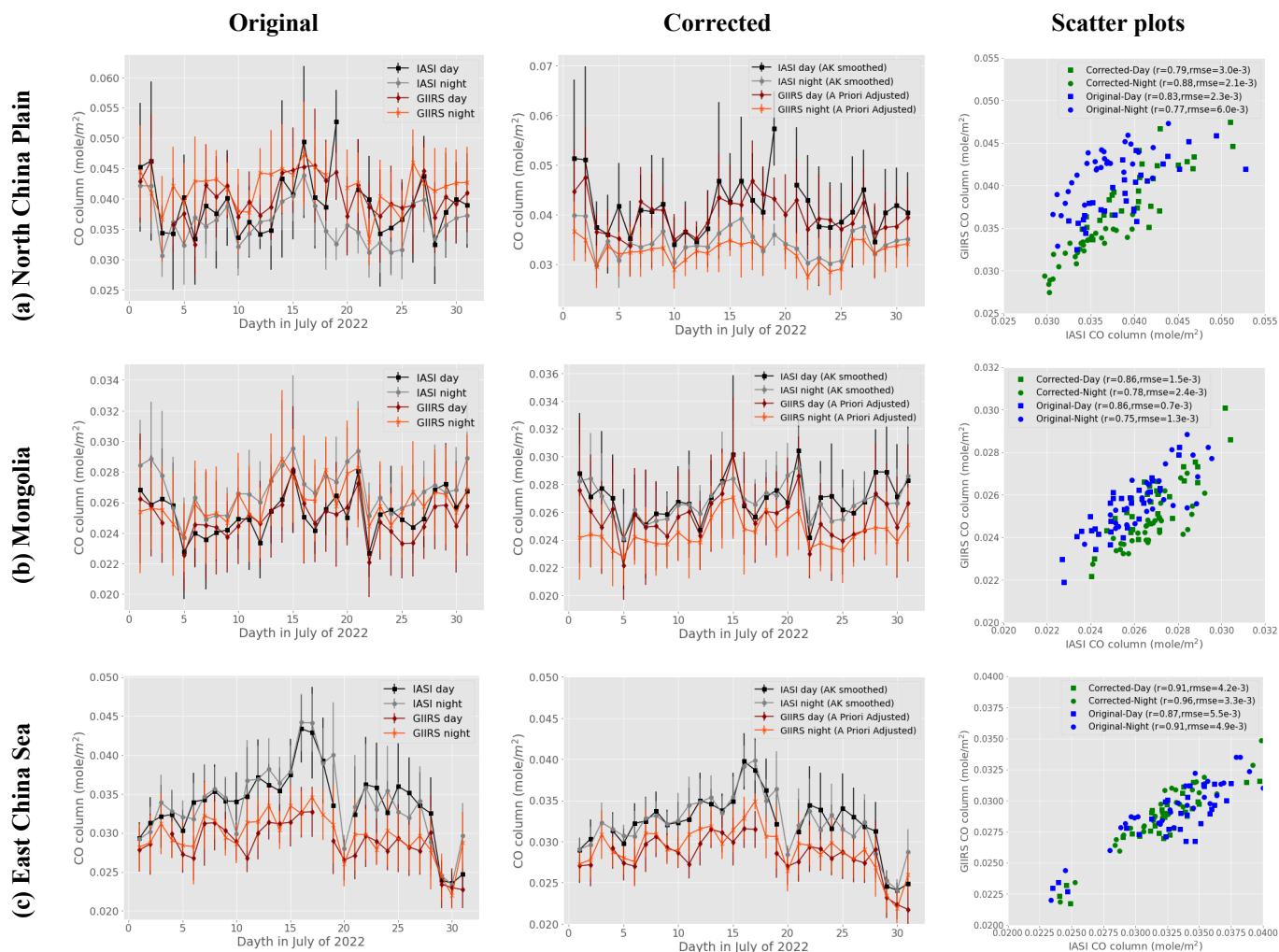
Figure 12: Comparison of time series of daily CO total column between GIIRS and IASI averaged over (a) North China Plain, (b) Mongolia, and (c) the East China Sea. GIIRS retrievals in the corresponding daytime and nighttime hours of IASI data are extracted. The first column shows a direct comparison of the retrievals; The second column shows the comparison after corrections, including a priori adjustment and AK matrix smoothing (see text for details). The third column shows their scatter plots, with correlation coefficients indicated.

7 Discussions

7.1 Improving the algorithm to detect CO from wildfires

Using spatially and temporally varying CO a priori, as in the current FY-GeoAIR algorithm, has the advantage of constraining CO in dense urban areas with persistently high emissions such as East Asia as demonstrated in this study. The algorithm's capability to capture anomalous events, such as wildfire CO emissions, remains to be tested. As suggested by **George et al. (2015)**, using such a priori with a smaller error range for $\mathbf{S}_a$, a strategy also adopted by MOPITT and TES retrieval algorithms, makes the retrieval system too tight to capture anomalously high or low CO values. Instead, the algorithm using a fixed a priori and a large error range for $\mathbf{S}_a$, such as the FORLI algorithm for IASI, is suggested to be more capable of detecting CO from anomalous events. Therefore, the FY-GeoAIR algorithm may be subject to adjustment in its a priori and its correlation matrix $\mathbf{S}_a$ for the purpose of detecting high CO emissions from wildfires.

7.2 Importance of AK smoothing for comparing retrievals

The importance of the AK matrix for intercomparison of retrievals has been described in detail by **Rodgers and Connor (2003)** using retrievals from MOPIIT, an LEO IR sounder, as an example of a space-born instrument. Because of the highly variable TC over the diverse land cover in East Asia, the GIIRS retrievals present distinctive vertical sensitivity for different hours at different locations, which makes the interpretation of the retrieval results more difficult and, therefore, better use of the AK matrix more important. For comparison with model simulations, as illustrated in the simulated synthetic experiments in **Sect. 5**, a correction as in **Eq. (9)** is necessary given the model simulated profile can be assumed to have uniform vertical sensitivity. For comparison with retrievals from other remote sounding instruments, which have different a priori and AK matrices, a two-step correction as in **Eq. (10)** and **Eq. (11)** is necessary to reconcile the retrievals. Because of the mismatch in observation footprints and the heterogeneity of the AK matrix over land, the collocation of sounding measurements from different instruments should also be carefully implemented to make sure the comparison is not biased due to inappropriate spatial interpolation.

8. Conclusions

495   Using hyperspectral infrared measurements from GIIRS onboard FY-4B, we showed the first results of diurnal CO, an important trace gas in the atmosphere, measured from a GEO orbit. The performance of the algorithm is first evaluated by conducting retrieval experiments using simulated synthetic spectra. Retrieval results from one month of GIIRS spectra in July 2022 show that the DOFS for the majority is between 0.6 and 1.2 for the CO total column and between 0 and 0.25 for the

500   bottom 0-1 km layer, which strongly depends on TC. Comparing the CO total column between GIIRS and IASI shows that the two datasets have good consistency in capturing the daily variabilities. These results demonstrate the capability of GIIRS in constraining the diurnal CO changes in East Asia. Since CO plays an important role in tropospheric atmospheric chemistry and is an effective tracer of CO_2, the CO retrievals at a spatial resolution of 12 km and a temporal resolution of 2 hours from GIIRS have great potential in improving local and global air quality and climate research. The operational geostationary

505   observation by GIIRS represents an important advancement over the once/twice-per-day observations provided by current LEO instruments.

    In the coming future, CO observations from planning GEO missions, e.g., ESA's IRS and NASA's GeoCarb, along with GIIRS onboard future Fengyun satellite series, will greatly expand our capability in monitoring global CO emissions at high temporal resolution across Asia, Europe, and America. Moreover, combining NIR and TIR to measure CO could further

510   improve constraining the CO profile from GEO orbits, as the NIR adds information in the boundary layer while the TIR is more capable of distinguishing near-surface and mid-troposphere (**Fu et al., 2016; Natraj et al., 2022**), which will be another very important advancement in the future.

Data availability

515 The CO retrieval data from FY-4B/GIIRS (https://doi.org/10.18170/DVN/M7DKKL) in this study are publicly available from the Peking University Open Research Data Platform at https://opendata.pku.edu.cn/; Future updates on FY-4B/GIIRS CO data will be posted on https://opendata.pku.edu.cn/dataverse/FYGEOAIR; FY-4B/GIIRS Level 1 data are publicly available from the FengYun Satellite Data Center at http://satellite.nsmc.org.cn/portalsite/default.aspx; IASI/Metop-B CO level 2 retrieval data are downloaded from IASI AERIs database portal at https://iasi.aeris-data.fr/co/; IASI is a joint mission of EUMETSAT

520 and the Centre National d'Etudes Spatiales (CNES, France). The authors acknowledge the AERIS data infrastructure for providing access to the IASI data in this study, ULB-LATMOS for the development of the retrieval algorithms, and Eumetsat/AC SAF for CO/O3 data production; The surface emissivity datasets are downloaded from the Global Infrared Land Surface Emissivity: UW-Madison Baseline Fit Emissivity Database at https://cimss.ssec.wisc.edu/iremis/; The ECMWF ERA5 reanalysis datasets are available from the Copernicus Climate Data Store at https://cds.climate.copernicus.eu/; The

525 ECMWF atmospheric composition datasets are available from the Copernicus Atmosphere Data Store at https://ads.atmosphere.copernicus.eu/.

Acknowledgment

Z.-C. Zeng acknowledges funding from the National Natural Science Foundation of China (No. 42275142) and the Fundamental Research Funds for the Central Universities, Peking University (No. 7101302981).

530 **Author contribution**

Z.Z. designed the study, developed the forward model and retrieval codes, carried out the experiments and results analysis, and prepared the manuscript. L.L. and C.Q. provided guidance on using the FY-4B/GIIRS L1 spectra data. All authors reviewed the manuscript.

Competing interest

535 The authors declare that they have no conflict of interest.

References

Bauduin, S., Clarisse, L., Theunissen, M., George, M., Hurtmans, D., Clerbaux, C., and Coheur, P.-F.: IASI's sensitivity to near-surface carbon monoxide (CO): Theoretical analyses and retrievals on test cases, J. Quant. Spectrosc. Ra., 189, 428–440, https://doi.org/10.1016/j.jqsrt.2016.12.022, 2017.

540 Borsdorff, T., Aan de Brugh, J., Hu, H., Aben, I., Hasekamp, O., and Landgraf, J.: Measuring carbon monoxide with TROPOMI: First results and a comparison with ECMWF- IFS analysis data, Geophys. Res. Lett., 45, 2826–2832, https://doi.org/10.1002/2018GL077045, 2018.

Brenninkmeijer, C. A. M. and Novelli, P. C.: Carbon monoxide, in: Encyclopedia Atmospheric Sciences, edited by: Holton, J. R., Academic Press, an imprint of Elsevier Science, London, 2389– 2396, 2003.

545 Buchwitz, M., de Beek, R., Noël, S., Burrows, J. P., Bovensmann, H., Bremer, H., Bergamaschi, P., Körner, S., and Heimann, M.: Carbon monoxide, methane and carbon dioxide columns retrieved from SCIAMACHY by WFM-DOAS: year 2003 initial data set, Atmos. Chem. Phys., 5, 3313–3329, https://doi.org/10.5194/acp-5-3313-2005, 2005.

Chin, M., Jacob, D. J., Munger, J. W., Parrish, D. D., and Dod- dridge, B. G.: Relationship of ozone and carbon monoxide over North America, J. Geophys. Res., 99, 565–573, 1994.

550 Clarisse, L., Van Damme, M., Hurtmans, D., Franco, B., Clerbaux, C., and Coheur, P. F.: The diel cycle of NH3 observed from the FY-4A Geostationary Interferometric Infrared Sounder (GIIRS), Geophys. Res. Lett., 48, e2021GL093010, https://doi.org/10.1029/2021GL093010, 2021.

Clarisse, L., Shephard, M. W., Dentener, F., Hurtmans, D., Cady- Pereira, K., Karagulian, F., Van Damme, M., Clerbaux, C., and Coheur, P.-F.: Satellite monitoring of ammonia: A case study of the San Joaquin Valley, J. Geophys. Res., 115, 555 https://doi.org/10.1029/2009JD013291, 2010.

Clerbaux, C., Hadji-Lazaro, J., Turquety, S., Mégie, G., and Coheur, P.-F.: Trace gas measurements from infrared satellite for chemistry and climate applications, Atmos. Chem. Phys., 3, 1495–1508, https://doi.org/10.5194/acp-3-1495-2003, 2003.

Clough, S. A., M. W. Shephard, E. J. Mlawer, J. S. Delamere, M. J. Iacono, K. Cady-Pereira, S. Boukabara, and P. D. Brown, Atmospheric radiative transfer modeling: a summary of the AER codes, Short Communication, J. Quant. Spectrosc. Radiat. 560 Transfer, 91, 233-244, 2005.

Clough, S. A., Shephard, M. W., Worden, J., Brown, P. D., Worden, H. M., Luo, M., Rodgers, C. D., Rinsland, C. P., Goldman, A., and Brown, L.: Forward model and Jacobians for tropospheric emission spectrometer retrievals, IEEE T. Geosci. Remote, 44, 1308–1323, 2006.

Crevoisier, C.: Use of Hyperspectral Infrared Radiances to Infer Atmospheric Trace Gases, Comprehensive Remote 565 Sensing, 7(2018), 345-387, 2018.

Crevoisier, C., Clerbaux, C., Guidard, V., Phulpin, T., Armante, R., Barret, B., Camy-Peyret, C., Chaboureau, J.-P., Coheur, P.-F., Crépeau, L., Dufour, G., Labonnote, L., Lavanant, L., Hadji-Lazaro, J., Herbin, H., Jacquinet-Husson, N., Payan, S., Péquignot, E., Pierangelo, C., Sellitto, P., and Stubenrauch, C.: Towards IASI-New Generation (IASI-NG): impact of improved spectral resolution and radiometric noise on the retrieval of thermodynamic, chemistry and climate variables, Atmos. Meas. 570 Tech., 7, 4367–4385, https://doi.org/10.5194/amt-7-4367-2014, 2014.

Deeter, M. N., Edwards, D. P., Gille, J. C., Emmons, L. K., Francis, G., Ho, S.-P., Mao, D., Masters, D., Worden, H., Drummond, J. R., and Novelli, P. C.: The MOPITT version 4 CO product: Algorithm enhancements, validation, and long-term stability, J. Geophys. Res.-Atmos., 115, D07306, https://doi.org/10.1029/2009JD013005, 2010.

Deeter, M. N., Emmons, L. K., Francis, G. L., Edwards, D. P., Gille, J. C., Warner, J. X., Khattatov, B., Ziskin, D., Lamarque, 575 J.-F., Ho, S.-P., Yudin, V., Attié, J.-L., Packman, D., Chen, J., Mao, D., and Drummond, J. R.: Operational carbon monoxide retrieval al- gorithm and selected results for the MOPITT instrument, J. Geo- phys. Res., 108(D14), 4399, https://doi.org/10.1029/2002JD003186, 2003.

De Wachter, E., Barret, B., Le Flochmoën, E., Pavelin, E., Matricardi, M., Clerbaux, C., Hadji-Lazaro, J., George, M., Hurtmans, D., Coheur, P.-F., Nedelec, P., and Cammas, J. P.: Retrieval of MetOp-A/IASI CO profiles and validation with 580 MOZAIC data, Atmos. Meas. Tech., 5, 2843–2857, https://doi.org/10.5194/amt-5-2843-2012, 2012.

ECMWF, 2022, CAMS global inversion-optimised greenhouse gas fluxes and concentrations, available at: https://ads.atmosphere.copernicus.eu/cdsapp#!/dataset/cams-global-greenhouse-gas-inversion

Forster, C., Wandinger, W., Wotawa, G., James, P., Mattis, I., Althausen, D., Simmonds, P., O'Doherty, S., Jennings, S. G., Kleefeld, C., Schneider, J., Trickl, T., Kreipl, S., Ja¨ger, H., and Stohl, A.: Transport of boreal forest fire emissions from 585 Canada to Europe, J. Geophys. Res., 106, 887–906, 2001.

Fu, D., Bowman, K. W., Worden, H. M., Natraj, V., Worden, J. R., Yu, S., Veefkind, P., Aben, I., Landgraf, J., Strow, L., and Han, Y.: High-resolution tropospheric carbon monoxide profiles retrieved from CrIS and TROPOMI, Atmos. Meas. Tech., 9, 2567–2579, https://doi.org/10.5194/amt-9-2567-2016, 2016.

Gambacorta, A., Barnet, C., Wolf, W., King, T., Maddy, E., Strow, L., Xiong. X., Nalli, N., and Goldberg, M.: An experiment 590 using high spectral resolution CrIS measurements for atmospheric trace gases: carbon monoxide retrieval impact study, IEEE Geosci. Remote Sens. Lett., 11, 9, 1639–1643, https://doi.org/10.1109/LGRS.2014.2303641, 2014.

Gambacorta, A., and Barnet, C. D.: Atmospheric Soundings from Hyperspectral Satellite Observations. Comprehensive Remote Sensing, 64–96. https://doi.org/10.1016/b978-0-12-409548-9.10384-7, 2018.

Gamnitzer, U., Karstens, U., Kromer, B., Neubert, R. E. M., Meijer, H. A. J., Schroeder, H., and Levin, I.: Carbon monoxide: 595 A quantitative tracer for fossil fuel CO2, J. Geophys. Res.-Atmos., 111, 1–19, https://doi.org/10.1029/2005JD006966, 2006.

George, M., Clerbaux, C., Hurtmans, D., Turquety, S., Coheur, P.- F., Pommier, M., Hadji-Lazaro, J., Edwards, D. P., Worden, H., Luo, M., Rinsland, C., and McMillan, W.: Carbon monoxide distributions from the IASI/METOP mission: evaluation with other space-borne remote sensors, Atmos. Chem. Phys., 9, 8317–8330, https://doi.org/10.5194/acp-9-8317-2009, 2009.

George, M., Clerbaux, C., Bouarar, I., Coheur, P.-F., Deeter, M. N., Edwards, D. P., Francis, G., Gille, J. C., Hadji-Lazaro, J., 600 Hurtmans, D., Inness, A., Mao, D., and Worden, H. M.: An examination of the long-term CO records from MOPITT and IASI: comparison of retrieval methodology, Atmos. Meas. Tech., 8, 4313–4328, https://doi.org/10.5194/amt-8-4313-2015, 2015.

Goldberg, M. D., Kilcoyne, H., Cikanek, H., and Mehta, A.: Joint Polar Satellite System: The United States next generation civilian polar-orbiting environmental satellite system, J. Geophys. Res.-Atmos., 118, 13463–13475, https://doi.org/10.1002/2013JD020389, 2013.

605 Hersbach, H., Bell, B., Berrisford, P., Hirahara, S., Horányi, A., Muñoz-Sabater, J., Nicolas, J., Peubey, C., Radu, R., Schepers, D., Simmons, A., Soci, C., Abdalla, S., Abellan, X., Balsamo, G., Bechtold, P., Biavati, G., Bidlot, J., Bonavita, M., De Chiara, G., Dahlgren, P., Dee, D., Diamantakis, M., Dragani, R., Flemming, J., Forbes, R., Fuentes, M., Geer, A., Haimberger, L., Healy, S., Hogan, R. J., Hólm, E., Janisková, M., Keeley, S., Laloyaux, P., Lopez, P., Lupu, C., Radnoti, G., de Rosnay, P., Rozum, I., Vamborg, F., Villaume, S., and Thépaut, J. N.: The ERA5 global reanalysis, Q. J. Roy. Meteor. Soc., 146, 1999– 610 2049, https://doi.org/10.1002/qj.3803, 2020.

Holmlund, K., Grandell, J., Schmetz, J., Stuhlmann, R., Bojkov, B., Munro, R., Lekouara, M., Coppens, D., Viticchie, B., August, T., Theodore, B., Watts, P., Dobber, M., Fowler, G., Bojinski, S., Schmid, A., Salonen, K., Tjemkes, S., Aminou, D., and Blythe, P.: Meteosat Third Generation (MTG): Continuation and innovation of observations from geostationary orbit, B. Am. Meteorol. Soc., 102, E990–E1015, https://doi.org/10.1175/BAMS-D-19-0304.1, 2021.

615 Hurtmans, D., Coheur, P.-F., Wespes, C., Clarisse, L., Scharf, O., Clerbaux, C., Hadji-Lazaro, J., George, M., and Turquety, S.: FORLI radiative transfer and retrieval code for IASI, J. Quant. Spectrosc. Ra., 113, 1391–1408, https://doi.org/10.1016/j.jqsrt.2012.02.036, 2012.

Ingmann, P., B. Veihelmann, J. Langen, D. Lamarre, H. Stark, and G. B. Courrèges- Lacoste: Requirements for the GMES atmosphere service and ESA's implementation concept: Sentinels-4/-5 and -5p. Remote Sens. Environ., 120, 58–69, 620 https://doi.org/10.1016/j.rse.2012.01.023, 2012.

Inness, A., Ades, M., Agustí-Panareda, A., Barré, J., Benedictow, A., Blechschmidt, A.-M., Dominguez, J. J., Engelen, R., Eskes, H., Flemming, J., Huijnen, V., Jones, L., Kipling, Z., Massart, S., Parrington, M., Peuch, V.-H., Razinger, M., Remy, S., Schulz, M., and Suttie, M.: The CAMS reanalysis of atmospheric composition, Atmos. Chem. Phys., 19, 3515–3556, https://doi.org/10.5194/acp-19-3515-2019, 2019.

625   Kim, J., Jeong, U., Ahn, M. H., Kim, J. H., Park, R. J., Lee, H., Song, C. H., Choi, Y. S., Lee, K. H., Yoo, J. M., Jeong, M. J., Park, S. K., Lee, K. M., Song, C. K., Kim, S. W., Kim, Y. J., Kim, S. W., Kim, M., Go, S., Liu, X., Chance, K., Miller, C. C., Al-Saadi, J., Veihelmann, B., Bhartia, P. K., Torres, O., Abad, G. G., Haffner, D. P., Ko, D. H., Lee, S. H., Woo, J. H., Chong, H., Park, S. S., Nicks, D., Choi, W. J., Moon, K. J., Cho, A., Yoon, J., Kim, S. kyun, Hong, H., Lee, K., Lee, H., Lee, S., Choi, M., Veefkind, P., Levelt, P. F., Edwards, D. P., Kang, M., Eo, M., Bak, J., Baek, K., Kwon, H. A., Yang, J., Park, J., Han, K.
630   M., Kim, B. R., Shin, H. W., Choi, H., Lee, E., Chong, J., Cha, Y., Koo, J. H., Irie, H., Hayashida, S., Kasai, Y., Kanaya, Y., Liu, C., Lin, J., Crawford, J. H., Carmichael, G. R., Newchurch, M. J., Lefer, B. L., Herman, J. R., Swap, R. J., Lau, A. K. H., Kurosu, T. P., Jaross, G., Ahlers, B., Dobber, M., McElroy, C. T. and Choi, Y.: New era of air quality monitoring from space: Geostationary environment monitoring spectrometer (GEMS), Bull. Am. Meteorol. Soc., 101(1), E1–E22, https://doi.org/10.1175/BAMS-D-18-0013.1, 2020.

635   Kobayashi, H., Shimota, A., Yoshigahara, C., Yoshida, I., Uehara, Y., and Kondo, K.: Satellite-borne high-resolution FTIR for lower atmosphere sounding and its evaluation, IEEE Trans. Geosci. and Remote Sens., 37, 1496–1507, http://dx.doi.org/10.1109/36.763262,1999.

Lai, R., Teng, S., Yi, B., Letu, H., Min, M., Tang, S., Liu, C: Comparison of Cloud Properties from Himawari-8 and FengYun-4A Geostationary Satellite Radiometers with MODIS Cloud Retrievals. Remote Sens., 11, 1703,
640   https://doi.org/10.3390/rs11141703, 2009.

Li, L., Ni Z., Qi, C., Yang, L., Han, C.:, Pre-Launch Radiometric Calibration of Geostationary Interferometric Infrared Sounder on FengYun-4B Satellite, Acta Optica Sinica, 42(6), 2022.

Luo, M., Rinsland, C. P., Rodgers, C. D., Logan, J. A., Worden, H., Kulawik, S., Eldering, A., Goldman, A., Shephard, M. W., Gunson, M., and Lampel, M.: Comparison of carbon monoxide measurements by TES and MOPITT: Influence of a priori
645   data and instrument characteristics on nadir atmospheric species retrievals, J. Geophys. Res.-Atmos., 112, D09303, https://doi.org/10.1029/2006JD007663, 2007.

Masuda, K., Takashima, T., and Takayama, Y.: Emissivity of pure and sea waters for the model sea surface in the infrared window regions, Remote Sens. Environ., 24, 313–329, https://doi.org/10.1016/0034-4257(88)90032-6, 1988.

Natraj, V., Luo, M., Blavier, J.-F., Payne, V. H., Posselt, D. J., Sander, S. P., Zeng, Z.-C., Neu, J. L., Tremblay, D., Wu, L.,
650   Roman, J. A., Wu, Y.-H., and Dorsky, L. I.: Simulated multispectral temperature and atmospheric composition retrievals for the JPL GEO-IR Sounder, Atmos. Meas. Tech., 15, 1251–1267, https://doi.org/10.5194/amt-15-1251-2022, 2022.

Noël, S., Reuter, M., Buchwitz, M., Borchardt, J., Hilker, M., Schneising, O., Bovensmann, H., Burrows, J. P., Di Noia, A., Parker, R. J., Suto, H., Yoshida, Y., Buschmann, M., Deutscher, N. M., Feist, D. G., Griffith, D. W. T., Hase, F., Kivi, R., Liu, C., Morino, I., Notholt, J., Oh, Y.-S., Ohyama, H., Petri, C., Pollard, D. F., Rettinger, M., Roehl, C., Rousogenous, C., Sha,
655   M. K., Shiomi, K., Strong, K., Sussmann, R., Té, Y., Velazco, V. A., Vrekoussis, M., and Warneke, T.: Retrieval of greenhouse gases from GOSAT and GOSAT-2 using the FOCAL algorithm, Atmos. Meas. Tech., 15, 3401–3437, https://doi.org/10.5194/amt-15-3401-2022, 2022.

O'Dell, C. W., Connor, B., Bösch, H., O'Brien, D., Frankenberg, C., Castano, R., Christi, M., Eldering, D., Fisher, B., Gunson, M., McDuffie, J., Miller, C. E., Natraj, V., Oyafuso, F., Polonsky, I., Smyth, M., Taylor, T., Toon, G. C., Wennberg, P. O.,
660   and Wunch, D.: The ACOS CO2 retrieval algorithm – Part 1: Description and validation against synthetic observations, Atmos. Meas. Tech., 5, 99–121, https://doi.org/10.5194/amt-5-99-2012, 2012.

Polonsky, I. N., O'Brien, D. M., Kumer, J. B., O'Dell, C. W., and the geoCARB Team: Performance of a geostationary mission, geoCARB, to measure CO2, CH4 and CO column-averaged concentrations, Atmos. Meas. Tech., 7, 959–981, https://doi.org/10.5194/amt-7-959-2014, 2014.

665   Rodgers, C. D.: Inverse Methods for Atmospheric Sounding: Theory and Practice, World Scientific, Singapore, 2000.

Rodgers, C. D. and Connor, B. J.: Intercomparison of remote sounding instruments, J. Geophys. Res., 108, 4116, https://doi.org/10.1029/2002jd002299, 2003.

Schmit, T. J., Li, J., Ackerman, S. A., and Gurka, J. J.: High- spectral- and high-temporal-resolution infrared measurements from geostationary orbit, J. Atmos. Ocean. Tech., 26, 2273– 2292, https://doi.org/10.1175/2009JTECHA1248.1, 2009.

670   Seemann, S. W., Borbas, E. E., Knuteson, R. O., Stephenson, G. R., and Huang, H.-L.: Development of a Global Infrared Land Surface Emissivity Database for Application to Clear Sky Sounding Retrievals from Multi-spectral Satellite Radiance Measurements, J. Appl. Meteorol. Clim., 47, 108–123, https://doi.org/10.1175/2007JAMC1590.1, 2008.

Shephard, M. W., McLinden, C. A., Cady-Pereira, K. E., Luo, M., Moussa, S. G., Leithead, A., Liggio, J., Staebler, R. M., Akingunola, A., Makar, P., Lehr, P., Zhang, J., Henze, D. K., Millet, D. B., Bash, J. O., Zhu, L., Wells, K. C., Capps, S. L.,
675   Chaliyakunnel, S., Gordon, M., Hayden, K., Brook, J. R., Wolde, M., and Li, S.-M.: Tropospheric Emission Spectrometer (TES) satellite observations of ammonia, methanol, formic acid, and carbon monoxide over the Canadian oil sands: validation and model evaluation, Atmos. Meas. Tech., 8, 5189–5211, https://doi.org/10.5194/amt-8-5189-2015, 2015.

Turner, D. S.: Systematic errors inherent in the current modeling of the reflected downward flux term used by remote sensing models, Appl. Opt., 43, 2369–2383, 2004.

680   Worden, H. M., Deeter, M. N., Frankenberg, C., George, M., Nichi- tiu, F., Worden, J., Aben, I., Bowman, K. W., Clerbaux, C., Co- heur, P. F., de Laat, A. T. J., Detweiler, R., Drummond, J. R., Edwards, D. P., Gille, J. C., Hurtmans, D., Luo, M., Martínez- Alonso, S., Massie, S., Pfister, G., and Warner, J. X.: Decadal record of satellite carbon monoxide observations, Atmos. Chem. Phys., 13, 837–850, https://doi.org/10.5194/acp-13-837-2013, 2013.

Yang, J., Zhang, Z., Wei, C., Lu, F., and Guo, Q.: Introducing the new generation of Chinese geostationary weather satellites,
685   Fengyun-4, B. Am. Meteorol. Soc., 98, 1637–1658, https://doi.org/10.1175/BAMS-D-16-0065.1, 2017.

Zeng, Z.-C., Zhang, Q., Natraj, V., Margolis, J. S., Shia, R.-L., Newman, S., Fu, D., Pongetti, T. J., Wong, K. W., Sander, S. P., Wennberg, P. O., and Yung, Y. L.: Aerosol scattering effects on water vapor retrievals over the Los Angeles Basin, Atmos. Chem. Phys., 17, 2495–2508, https://doi.org/10.5194/acp-17-2495-2017, 2017.

Zeng, Z.-C., Natraj, V., Xu, F., Chen, S., Gong, F.-Y., Pongetti, T. J., Sung, K., Toon, G., Sander, S. P., and Yung, Y. L.:
690   GFIT3: a full physics retrieval algorithm for remote sensing of greenhouse gases in the presence of aerosols, Atmos. Meas. Tech., 14, 6483–6507, https://doi.org/10.5194/amt-14-6483-2021, 2021.

Zoogman, P., Liu, X., Suleiman, R., Pennington, W., Flittner, D., Al-Saadi, J., Hilton, B., Nicks, D., Newchurch, M., Carr, J., Janz, S., Andraschko, M., Arola, A., Baker, B., Canova, B., Miller, C. C., Cohen, R., Davis, J., Dussault, M., Edwards, D., Fishman, J., Ghulam, A., Abad, G. G., Grutter, M., Herman, J., Houck, J., Jacob, D., Joiner, J., Kerridge, B., Kim, J., Krotkov,
695   N., Lamsal, L., Li, C., Lindfors, A., Martin, R., McElroy, C., McLinden, C., Natraj, V., Neil, D., Nowlan, C., O'Sullivan, E., Palmer, P., Pierce, R., Pippin, M., Saiz-Lopez, A., Spurr, R., Szykman, J., Torres, O., Veefkind, J., Veihelmann, B., Wang, H., Wang, J., and Chance, K.: Tropospheric emissions: Monitoring of pollution (TEMPO), J. Quant. Spectrosc. Ra., 186, 17–39, https://doi.org/10.1016/j.jqsrt.2016.05.008, 2017.

700 **Appendix A**
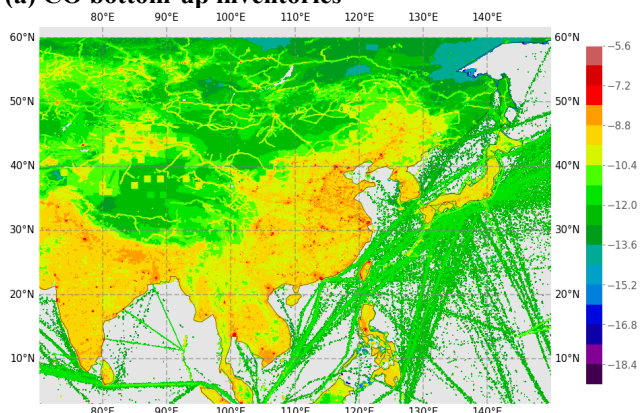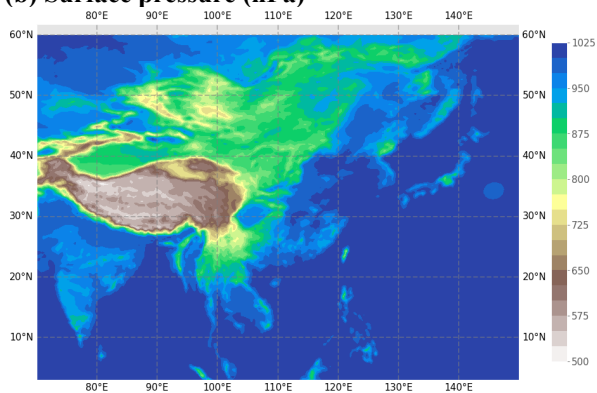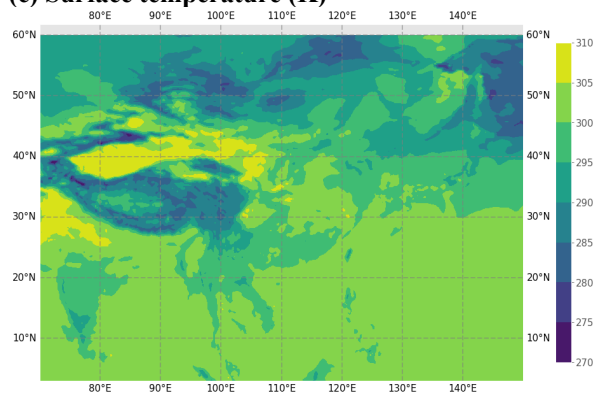
Figure A1: (a) Bottom-up estimated CO emissions on July 07, 2022, from the CAMS model. These emissions include anthropogenic CO emissions from fossil fuel use on land, shipping, and aviation, and natural CO emissions from vegetation, soil, the ocean, and termites. The emissions are in a unit of [kg m^{-2} s^{-1}] at log$_e$10 scale; (b) Surface pressure from ECMWF ERA5 reanalysis for the surface layer; (c) The surface temperature from ECMWF ERA5 reanalysis for the surface layer.